Dissertation

submitted to the
Combined Faculties for the Natural Science and for Mathematics
of the Ruperto-Carola University of Heidelberg, Germany
for the degree of
Doctor of Natural Sciences

presented by
Diploma-Physicist Cristina Alvarez Diez
born in Böblingen

Oral examination: October 18, 2006

A 3-sided Pyramid Wavefront Sensor controlled by a Neural Network for Adaptive Optics

to reach diffraction-limited imaging of the retina

Referees: Prof. Dr. Josef Bille
Prof. Dr. Karl-Heinz Brenner

Zusammenfassung

In-vivo Bildaufnahmen der Netzhaut sind in der Ophthalmologie die Grundlage zur Diagnose retinaler Erkrankungen. Die Auflösung der Bilder ist jedoch – neben der unvermeidbaren Beugungsbegrenzung aufgrund der endlichen Pupillengröße – durch die nicht perfekten, Aberrationen hervorrufenden, optischen Elemente des Auges eingeschränkt. In der Astronomie bestätigten erste Testmessungen von atmosphärischen Aberrationen mit dem neuartigen 4-seitigen Pyramidensensor die Vorteile dieses Sensors gegenüber konventionellen Wellenfrontsensoren. Diese Arbeit stellt einen Pyramiden-Wellenfrontsensor vor, der die Messung von Aberrationen und ihre Kompensation an einem konfokalen Laser Scanning Ophthalmoskop ermöglicht. Hierfür wird jedoch ein 3-seitiges Pyramidenprisma verwendet und experimentell gezeigt, daß dieses Prisma, das einfacher in der Herstellung ist als das 4-seitige Prisma, einen gleichwertigen Sensor darstellt.
Die Steuerung des deformierbaren Spiegels, welcher die Aberrationen kompensieren kann, wird durch ein künstliches neuronales Netz auf Basis der Sensordaten realisiert. Mit dem trainierten neuronalen Netz konnten Aberrationen von 150nm RMS bereits auf die Hälfte reduziert werden. Das neuronale Netz setzt sich zusammen aus einem *2*×4-schichtigen *convolutional* S_C-Netz, das Merkmale aus den Signalbildern der Pyramide extrahiert, und einem 3-schichtigen, iterativen Backpropagation-Netz, das die benötigte Deformation des Spiegels zur Korrektur einer gegebenen Aberration ermittelt.

Abstract

In-vivo imaging of the eye's fundus is the basis for the diagnosis of retinal diseases in ophthalmology. However, the resolution of the images is limited – besides the inevitable diffractive limitation by the finite size of the pupil – by the imperfect optical elements of the eye, causing aberrations. In astronomy, first test measurements of atmospheric aberrations with the novel 4-sided pyramid sensor have confirmed the benefits of this sensor compared with conventional wavefront sensors. This work presents a pyramid wavefront sensor for the measurement of aberrations and their compensation on a confocal laser scanning ophthalmoscope. By contrast, a 3-sided pyramid prism is used and it is demonstrated experimentally, that this prism, which is easier to manufacture than the 4-sided prism, reveals to be an equivalent sensor. The control of the deformable mirror which can compensate the aberrations is implemented by an artificial neural network based on the acquired sensor data. With the trained neural network, aberrations of 150nm RMS could already be reduced to half the error. The neural network is composed of a convolutional S_C-net of 2×4 layers, which extracts feature information out of the signal images of the pyramid, and a 3-layer, feed-forward backpropagation net, that determines the required deflection of the mirror in order to compensate for a given aberration.

"...alle Dinge ziehen durch eure Seele in beständiger Umarmung:
das Erwünschte und das Gefürchtete,
das Verabscheute und das Geliebte,
das Angestrebte und dasjenige, dem ihr entrinnen möchtet.
Diese Dinge bewegen sich in euch
als untrennbare Paare von Licht und Schatten.
Und wenn ein Schatten verblasst und verschwindet,
wird das verbleibende Licht
zum Schatten eines anderen Lichtes."

Khalil Gibran – Von der Freiheit

Contents

Chapter 1

Introduction

Wavefront aberrations play an important and yet negative role during the acquisition of high resolution images. In cell microscopy this is due to the surrounding inhomogeneous aqueous; in astronomy due to turbulences in the atmosphere; in retina imaging due to the non-perfect optical apparatus: measuring the aberrations that distort the image quality and pre-compensating them, increases significantly the resolution of the desired image. The principle of such an adaptive optical system is the same in all cases: Wavefront aberrations that diminish the image quality of the object under investigation (cell, star, eye, etc.) are measured by a sensor. A controlling device translates this signal to an actuator which then compensates the aberrations. Thus, theoretically, the image's resolution can become just diffraction-limited.
For an application in ophthalmology adaptive optics have to be compact, handy and low-priced compared to systems used for example in astronomy.

A 3-sided pyramid prism was tested in this work as a wavefront sensor, where its signal was translated for correction not analytically but by an artificial neural network. The control unit thus was a computer which, via a trained neural net, calculates the must value of the actuator from the signals which have been measured before by the sensor.
4-sided pyramid prisms for aberration measurements were introduced 1996 for astronomy by Ragazzoni [Rag96]. First investigations for ophthalmology with a pyramid sensor were done by Artal [Igl02] and recently by Dainty [Cha06]. First tests with a 3-sided prism were made at the Max-Planck Institute for Astronomy [Cos05].
This work presents a 3-sided prism pyramid wavefront sensor used in the most sensitive mode, the so-called unmodulated mode, and with a controller for the servo-loop being an artificial neural network.

The advantage of the pyramid sensor compared with other sensors such as

the Hartmann-Shack sensor, the Twyman-Green interferometer or the curvature sensor is its adjustable resolution by varying the sampling of the image signal and its adjustability of the gain, that is of the sensitivity. In modulation modus the pyramid sensor is less sensitive but able to measure even big aberrations. Modulation modus is when the wavefront - which is focused to the pyramids tip - is moved periodically around the tip. Diminishing the modulation amplitude while correcting, that is diminishing the aberrations, makes the pyramid sensor more sensitive as its gain is increased. For very small aberrations the amplitude can be zero. A calculation of the aberration in this non-modulating, sensitive regime is more complex than in the modulating mode and smallest misalignments or deviations from the parameters that were assumed in the calculation lead to inconsistency between theoretical prediction and experimental result. Thus if an adequate neural network can be found and trained to recognize the aberrations out of the pyramid sensor's signal (i.e. out of the three pupil images), any small misalignment or imperfection of the system optics and even noise would be taken into account.

This thesis shows how a neural network can be used for regulation of an adaptive optical system with a 3-sided pyramid prism as a wavefront sensor to integrate it in a laser scanning ophthalmoscope. Although the adaptive optical system can be used nearly identically in other scientific fields, this work was evolved for the application on in-vivo imaging of the human retina. It was developed for the integration in a scanning laser ophthalmoscope with a pre-compensator for aberrations of big amplitudes with a pair of lenses in a telescopic set-up for defocus and a phase-plate system [Zha05] for the remaining aberrations of big amplitude.

A wavefront sensor for integration in an adaptive optics scanning laser ophthalmoscope is presented in this work. With images of the retina of higher resolution, diseases can be recognized sooner by a medical doctor.
In accordance with the current work done in our group (phase plates correction, new methods of investigating properties of the retina) this is one more component to a low-price, simple-to-handle and optically high-quality adaptive optics scanning laser ophthalmoscope.

A brief introduction explaining the advantages and the idea of adaptive optics in ophthalmology will be given in the next chapter expounding the definition and description of wavefront aberrations. The third chapter begins with the geometrical description of the pyramid wavefront sensor before the precise formulation with diffractive optics is derived afterwards. Chapter 4 is

devoted to the actuators that are used in this work: a deformable membrane and a deformable segmented mirror.
The theoretical background about artificial neural networks which is necessary in order to understand the network that was constructed and trained, is presented in chapter 5.
In chapter 6 the laboratory set-up, consisting of the optical, the electronic and the software components and their interface that were developed are specified. The results of the work, the measurements with the pyramid sensor, the neural network training and the work done on a laser scanning ophthalmoscope at Moorfields Hospital in London are presented in chapter 7. In the last chapter a discussion of the results and their relevance is given. The work finishes with an outlook.

Chapter 2

Adaptive Optics for the Human Eye

Knowledge about the human eye, including the retina, is available in great detail through post mortem eyes in-situ imaging. Here, the histology of the retina or retinal diseases in their end-phase can be described in detail by microscopy up to a level of intra-cellular resolution.
This resolution cannot be achieved in a living eye by simple fundus imaging. The aberrations – introduced by the imperfect optics in addition to the finite entrance pupil of the iris – impede a similar resolution as attained with in-situ imaging. To overcome the former restriction, adaptive optics (AO) have to be integrated in intra-ocular imaging in order to compensate the deterioration by aberrations.

2.1 Application of Adaptive Optics in Ophthalmology

Scanning laser ophthalmoscopes (SLO) are frequently used in ophthalmology in a standard procedure to identify numerous diseases like glaucoma, diabetic retinopathy, macular holes, macular oedema or age related macular degeneration (AMD) [Bin06, Hud03, Rue98]. To obtain an image of the eye's fundus, pictures are recorded typically with a rate of 25 pictures per second. Afterwards noise reduction can be accomplished by a software program which averages over a set of e.g. 30 pictures returning an enhanced image. Investigation in adaptive optics for ophthalmology is done worldwide to reach maximum, i.e. diffraction limited, resolution of retinal images so that retinal diseases can be detected in their early stage of development and to obtain more detailed knowledge about the evolution of the diseases.

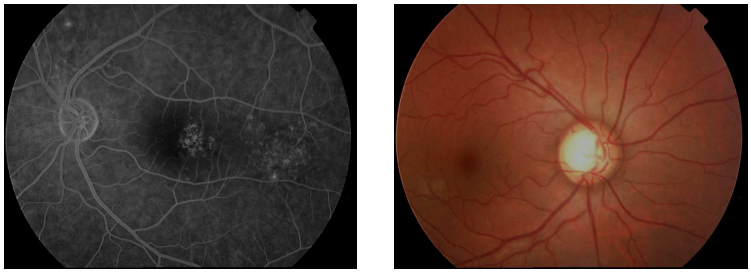

Figure 2.1: Averaged SLO images of the retina; left: fluorescine image of a fundus with AMD; right: papilla with glaucoma (both images courtesy of E.Jalil, Hospital Barros Luco, Santiago de Chile)

2.1.1 Scanning Laser Ophthalmoscope

A Scanning Laser Ophthalmoscope (SLO) scans a collimated laser beam horizontally and vertically. This is done with the scanner being conjugated to the pupil of the eye. It is the unaccommodated eye itself, that focuses the beam onto the retina to a spot. In this way, the spot intensity of the light that is back reflected from the retina is measured point by point obtaining a complete picture of the retina after one scanning cycle by means of a reconstruction software.
In the case of an optically perfect eye, 84% of the beam intensity [Ber03] would reach and be focused onto the retina to a spot of the size of the corresponding Airy-disc, thus being only diffraction-limited by the size of the pupil. However, for a normal eye, even an emmetrope one, imperfections

Figure 2.2: One single image from a z-scan (i.e. axial-scan), unaveraged, of the low temporal part of the optic nerve, taken with our laboratory Heidelberg Retina Tomograph.

of the optical components produce aberrations, so that the beam is focused to a bigger and misshapen spot which will consequently decrease the image resolution. Attempts to reach a better diffraction-limited resolution by increasing the pupil to its maximum size of 7 to 8mm diameter fail because of

the stronger distorting area more distant from the eye's optical axis.
The beam can reach diffraction-limited size only by pre-compensating these aberrations with an actuator in an AO system (see Sec. 2.3).

2.1.2 The light's path through the eye

Pictures of the retina are acquired by 2-dimensional scanning of a low power laser beam focused on the retina. "Pixel by pixel" the intensity of the back-scattered light is measured by a photodetector (photodiode or photomultiplier) forming a picture after one scanning cycle. The beam or any light that enters the eye when looking at an object has to pass various media of the eye before reaching the retina. The back reflected light has to pass the same eye components just in the opposite order before being measured by an apparatus after it exits the eye.

Light first passes through the cornea (Fig. 2.3) that gives the eye a power of refraction of 43 diopter. The cornea is covered with a tear film of 10μm, protecting the eye from drying out and giving the cornea an optically smooth surface. Each blinking renews the tear film distribution [Dub04]. The cornea itself is approximately 700μm thick, formed of 5 layers, the stroma with around 500μm being the thickest layer.

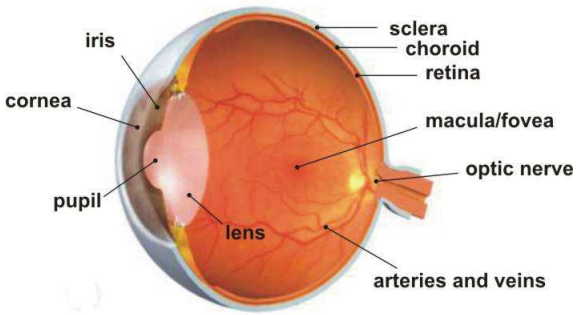

Figure 2.3: Anatomy of a right eye, cut vertically. (Modified from [InsAl])

After the cornea the light passes the anterior chamber filled with an aqueous humor before going through the pupil (the iris' aperture, with a diameter that varies between 1.5 and 8mm when adapting to bright or dark light) and reaching the lens. The lens is curved more on its back than on its front side. Its index of refraction is not homogeneous but increases from the surface to the core from 1.39 to 1.41. By changing the shape of the lens, accommodation to see far or near is accomplished. The possible variation in power of refraction by accommodation is 14 diopter in adolescents, decreasing

to 6 diopter and less for adults at an age above 40 [Kor94, Pat03].
The last path the light crosses before reaching the retina is the vitreous body, a viscid and transparent hydro-gel with a water consistency of 99%.

The retina itself consists of 10 layers. Their order is called 'inverse', as the photoreceptor layer with the colour distinguishing cones and the rods for seeing under low intensities is in the second to last layer (Fig. A.1). The light has to traverse first all inner lying layers before being detected by the photoreceptors and being converted into an electrical signal. This signal is transported in the opposite direction from the outer plexiform layer (a fiber layer with a multitude of synapses between the photoreceptors and the bipolar and horizontal cells of the inner nucleus layer) over the inner nucleus layer (also containing the amacrite cells and the cores of the Müller cells) to the layer of the ganglion cells where it is partly preprocessed. Finally, the signal reaches the nerve fiber layer, the axons of the ganglion cells. These fibers bundle to form the optic nerve where the signal is lead to the visual cortex of the brain.
The pigment epithelial layer has appendices and the ability to retract them in darkness and to protrude them in bright light to suppress light scattering. A more detailed description of retina layers' histophysiology can be found in standard textbooks of ophthalmology (e.g.[Jun96]).

Simple optical eye model

When making theoretical calculations, the approaches are usually done using an eye model having a length of 22.6mm from cornea to fundus. The term fundus is used for the layers of the retina, the choroid, and the sclera.

The cornea and the lens can be dealt with as one single optical system with its nodal point 17mm before the retina, and the principal point at the cornea, 5.6mm away from the nodal point; one focal point is located at the retina (fovea), the other focal point 17mm before the cornea.

Ocular and fundus reflection

Many fundus reflection models have been developed, an overview can be found in [Ber03]. To summarise, the following can be said:

At all interfaces of layers with different index of refraction a part of the beam intensity will be reflected. Ocular reflectors are the cornea, the lens and the fundus. The fundus has a reflectivity of approximately 4%, that is the added up reflectivity of the interfaces of sclera, of choroid, and of the retinal layers - being less for dark and more for bright eyes. The receptors reflectivity is said to originate from the disc stack [Kra96].

The reflected intensity of cornea and lens is higher than the intensity reflected at the fundus. Experimental set-ups for retinal imaging avoid this problem by confocal imaging. Thus, hardly any light reflected from a plane not originating from the retina passes the confocal pinhole to the detector.

2.1.3 Frequency dependence and eye tremors

To measure the aberrations of a human eye the patient is asked to fix his view to a target. A patient fixating on a target will still be moving his eye involuntarily, performing rotational and transversal movements.

Saccades are very fast movements of the eye with velocities up to 500°/sec when looking at an object and scanning all parts of importance so that they fall at the fovea for a sharp view. While for a patient with good fixation abilities saccades can be discarded, microsaccades, micro-fluctuations and involuntary small tremors, cannot. The origin of these small fluctuations of the eye's optics is not completely clear, but accommodation movements of the lens, pulsation and micro-movements preventing saturation of the receptors, among others, play a major role.

Hofer et al. [Hof01] measured a frequency dependence of the eye's aberrations for up to 10Hz and for Zernike modes (see Sec.2.2) up to the 5th order. They obtained a spectrum decreasing with approximately 4dB per octave, that is, for the frequency increasing by a factor of 10, the power of the aberrated light diminishes by a factor of $10^{\frac{4}{3}}$.

Another factor that can suddenly change the amount of aberration is a break-up of the tear film which happens after the break-up time t_{BUT} =10±5s in normal eyes if the patient does not blink. Directly after blinking the tear film is distributed homogeneously over the cornea. Lin et al. [Lin05] showed on a study with 50 emmetropic subjects, that with normal eyes having an average of 0.2μm the root mean square error (RMS) directly after blinking, RMS increases from 0.23μm at $t = \frac{1}{2}t_{BUT}$ to 0.3μm at the moment of tear film break-up. Thus, it is important to encourage the patient to blink normally to avoid this source of aberrations; otherwise the amplitude spectrum will get higher values for a extended width of the spectrum.

Ocular micro-tremor are very small, irregular movements of the eye between 150nm and 2μm (cornea displacement). This movements are caused by extra-ocular muscle stimulation. The ocular micro-tremor has a peak to peak mean frequency of 84Hz [Boj01].

According to the Nyquist theorem, a measurement of the micro-tremors and all other eye movements requires a wavefront sensing of at least double their frequency (around 200Hz). This shows the importance of sensors being

fast enough to follow signals of these frequencies.

2.1.4 Polarizing effects of the eye

When entering with a linear polarized beam into the eye, the reflected beam is not totally polarized anymore in the same direction. Reflected light generally changes its polarization according to Fresnel equation. However, in the case of a human eye the main contribution comes from the birefringence of the cornea, lens and retina. A measure for quantifying the change of polarization when the incident beam is linear polarized, is the so called degree of polarization dp. It is defined as

$$dp = \frac{I_{pol}}{I_{pol} + I_{unpol}} \tag{2.1}$$

with I_{pol} being the intensity of the polarized light, and I_{unpol} the intensity of the unpolarized light.

The stroma of the cornea consists of around 100 parallel aligned sheets causing the birefringent effect. The retardation is highest for a polarization oriented 15° in nasal-down direction. The lens birefringence is very small and can be neglected.
In the retina it is the retina nerve fiber layer (RNFL) which causes retardation. The RNFL consists of parallel ordered axon bundles containing microtubes. They have cylindrical organelles with a diameter smaller than an visible wavelength. The optical axis of the RNFL is parallel to its bundles, the optical axis being the slow axis of birefringence. Retardation is proportional to the thickness of the birefringent layer. As the RNFL is thicker above and below the optic disc and the axons are ordered radially, the retardation will be larger above and below the disc and will have a radial symmetry.

A similar effect happens at Henle's fiber layer. Henle's fiber layer is the outer plexiform layer in the region of the macula. It consists of elongated photoreceptor axons extending radially from the fovea. The layer is more uniform than the peripapillary RNFL [Hua03, Zho02]. The retardation effect of polarized light around the fovea can be observed with a polarizer-analyzer set-up, that is a polarizer in the input and output beam, respectively, with their axes in crossed orientation. It results in a double-brush like distribution of the intensity distribution, the so-called Haidinger brushes [Gre02].
The added retardation from the retina (measured at the fovea) and the cornea is around $\frac{1}{7}\lambda$ [Bue00], considering that all effects are wavelength dependent and differ particularly from person to person.

2.2 Wavefront Characterization

To pre-compensate the aberrations of the eye, the wavefront of the back-reflected light is measured. The wavefront is described mathematically by a set of Zernike coefficients.

2.2.1 Wavefront definition

From Maxwell's equations the wave equation

$$\bigtriangledown^2 u(\overrightarrow{r},t) - \frac{n^2}{c^2}\frac{\partial^2 u(\overrightarrow{r},t)}{\partial t^2} = 0 \tag{2.2}$$

can be derived, where the scalar $u(\overrightarrow{r},t)$ represents any vector component of the electric field $\overrightarrow{E}$ or of the magnetic field $\overrightarrow{H}$, n is the index of refraction, and c the velocity of light in free space. Regarding a monochromatic wave

$$u(\overrightarrow{r},t) = Re\left[u_r(\overrightarrow{r})\cdot e^{-i\omega t}\right]$$

we can substitute $u(\overrightarrow{r},t)$ in Eq. 2.2 and get the Helmholtz equation

$$(\nabla^2 + \frac{n^2}{c^2}\omega^2)u_r = (\nabla^2 + k^2)u_r = 0 \tag{2.3}$$

To describe a monochromatic wave in an inhomogeneous medium we rewrite the space dependent factor $u_r(\overrightarrow{r})$ of the above wave to

$$\begin{aligned} u_r(\overrightarrow{r}) &= \hat{u}_r(\overrightarrow{r})\cdot e^{i\varphi(\overrightarrow{r})} \\ &= \hat{u}_r(\overrightarrow{r})\cdot e^{i\frac{2\pi}{\lambda_0}S(\overrightarrow{r})} \end{aligned} \tag{2.4}$$

using $\varphi(\overrightarrow{r}) = \frac{2\pi}{\lambda_0}S(\overrightarrow{r})$ for the phase of the wave; λ_0 is the wavelength in free space of the monochromatic wave and $S(\overrightarrow{r})$ is the so-called eikonal. Planes with $S(\overrightarrow{r}) = const$ are called wavefronts. We can depict wavefronts as those planes which have constant phase, or – in terms of geometrical optics – those planes formed by all points with the same optical path distance of the corresponding ray from the source point.

Substituting Eq. 2.4 in the Helmholtz equation, and using the geometrical approximation $\frac{\nabla^2\hat{u}_r}{\hat{u}_r} \approx 0$ it can be shown [Goo05] that the so-called eikonal equation

$$|\nabla S(\overrightarrow{r})|^2 = n^2(\overrightarrow{r}) \tag{2.5}$$

emerges. The eikonal equation quantifies the relation between the wavefront

and the index of refraction of a medium. In the case of a human eye this explains not only the desired refraction of light on the surfaces of the cornea or of the lens but also the undesired arising of wavefront deformations caused by media or by surfaces which are not perfectly homogeneous or even by particles with a totally different index of refraction as they can be found e.g. in the vitreous body.

Hence, in the idea of light as wave, the wavefront is *that* surface in space where the electric (or magnetic) field has the same phase, which is in accordance with the geometrical formulation. A point source in free space would thus form the well known spherical wavefronts.
When talking about aberrations, one usually refers to the deviation of a wavefront from the ideal plane wavefront
$E(\overrightarrow{r},t) = Re(E_0 e^{i(\omega t - \overrightarrow{k}\,\overrightarrow{r}+\xi)} = Re(E_0 e^{i\phi(\overrightarrow{r},t)})$
or the ideal spherical wavefront
$E(\overrightarrow{r},t) = Re(\frac{E_0}{|\overrightarrow{r}|} e^{i(\omega t - \overrightarrow{k_r}\,\overrightarrow{r}+\xi)} = Re(\frac{E_0}{|\overrightarrow{r}|} e^{i\phi(\overrightarrow{r},t)})$
where the phase $\phi(\overrightarrow{r},t)$ forms flat planes and spherical surfaces, respectively, of constant value for $t = const$ (E_0: amplitude, ξ: constant phase factor, $\overrightarrow{k}$: wave vector, ω: wave frequency).
In this work we will refer to the plane wavefront when talking about aberrations.

2.2.2 Zernike polynomials

To describe mathematically a wavefront, we have to find a function mapping from the 2-dimensional space to the 1-dimensional space. This function can be decomposed in any complete set of orthogonal functions. For wavefront aberrations with circular aperture and specially for application in ophthalmology, the representation by Zernike polynomials Z_n^m is very convenient as the first polynomials include defocus and astigmatism, with which the biggest part of an eye's aberration [Cas02] can be formulated. The indices m and n represent the azimuthal frequency and the radial order, respectively. The general formulation of the Zernike polynomials in polar coordinates with radius ρ and angle ϕ is

$$Z_n^m(\rho,\phi) = \begin{cases} R_n^{-m}(\rho) sin(m\phi); & m < 0 \\ R_n^{m}(\rho); & m = 0 \\ R_n^{+m}(\rho) cos(m\phi); & m > 0 \end{cases} \tag{2.6}$$

with the term R_n^m, which depends only from the radius, being

$$R_n^m(\rho) = \sum_{i=0}^{(n-m)/2} \frac{(-1)^i (n-i)!}{s!(\frac{n+m}{2}-i)!(\frac{n-m}{2}-i)!} \cdot \rho^{n-2i} \tag{2.7}$$

A function $f(\rho, \phi)$ can now be represented with this polynomial set using the corresponding coefficients c_n^m:

$$f(\rho, \phi) = \sum_{n,|m|=0}^{\infty} c_n^m \cdot Z_n^m(\rho, \phi) \tag{2.8}$$

In Appendix B the first 14 Zernike polynomials are formulated and illustrated graphically. The indexation is changed there from Z_n^m to one index Z_k, with $k = \frac{1}{2}(n(n+2)+m)$. The defocus polynomial Z_2^0 for example, changes to Z_4.

A single number to quantify, obviously very roughly, the magnitude of aberrations of a wavefront is the Strehl ratio S. It is the ratio between the intensity of the image at the optical axis ($x' = 0, y' = 0$) and the intensity at the same point in the case of an ideal, aberration-free image.

$$S = \frac{I_{ab}(x' = 0, y' = 0)}{I_{ideal}(x' = 0, y' = 0)} \tag{2.9}$$

2.3 Closed-loop Systems in Ocular Adaptive Optics

Adaptive optics (AO) have been developed since the 1970's with the aim to apply them for military and astronomic purpose, obviously starting with much simpler devices than today [BiN73, Mik73]. It was not before the middle of the 1990's [Lia97] that AO were implemented in ophthalmology after progress had been made in ocular wavefront sensing [BiL94].

As for any closed-loop, 3 modules are necessary to improve the image quality (Fig. 2.4): a sensor measuring the variable of the control path to be controlled, an actuator that compensates the deviation of the variable from its must-value, and a controller which extracts from the signal that the sensor has measured the behaviour which the actuator has to follow. For AO, to correct wavefront aberrations, there are several possible closed-loop systems, as there are different combination possibilities, depending on which type of actuator (membrane mirror, segmented mirror, liquid crystal modulator (Chap. 4)), which kind of sensor (Hartmann-Shack, curvature sensor, interferometer, pyramid sensor (Chap. 3)) or which kind of controller is used. The controller is usually a computer, which either can supervise the loop by analytical or numerical calculation from the sensor's signal, or by a trained neural network.

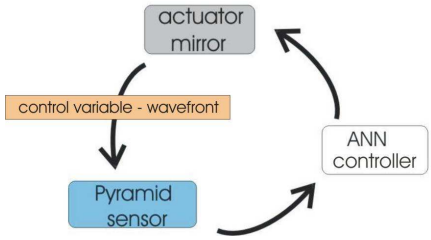

Figure 2.4: Closed-loop diagram

Although one of the 3 components may be quite fast, the slowest component determines the bandwidth of the overall system. Besides, the correction of the wavefront is not done in one cycle. Even if the exact aberration could be measured at once, control theory shows [Sch03], that for stability reasons, the correction is not possible with any arbitrary frequency and especially it is not possible to correct the deviation in one step. Therefore several loops are required to correct the wavefront to the optimum. The system's bandwidth is thus given by the bandwidth of one loop divided by the number of loops required to reach full correction.
That is the reason why in all works done until now, closed-loop for ocular systems achieved bandwidths of 5Hz [Fer01, Hof01] and 12Hz [Dia03] although the wavefront measurement can be done with frequencies up to 50Hz and 240Hz respectively, and even >300Hz [Nir05] using in all cases a Hartmann-Shack sensor.

This work is done for developing an AO system with a 3-sided pyramid prism as sensor, a neural net as controller and a membrane mirror as actuator, to integrate it in the Heidelberg Engineering Tomograph (HRT), a confocal scanning laser ophthalmoscope (cSLO). The first implementation of an AO system in a cSLO was done by Roorda et al. [Roo02] with a single loop frequency of 30Hz. They achieved a RMS of $0.12\mu m$ over a 7mm pupil with a lateral resolution of $2.5\mu m$ which is double the resolution that is given by a conventional cSLO (HRT) without AO [HE04].

The pyramid sensor was first applied for ophthalmology by Iglesias et al. [Igl02]. They used a modified 4-sided pyramid to measure the optical aberrations up to 4th order of Zernike polynomials. Chamot et al. [Cha06] presented recently the first application of the pyramid sensor (also a 4-sided one) in AO for the eye, achieving a RMS of $0.14\mu m$ over a 6mm pupil.

Chapter 3

The Pyramid Wavefront Sensor

Different sensors are available to measure the aberrations of a wavefront: The curvature sensor, the Hartmann-Shack sensor, the Twyman-Green interferometer, and the pyramid sensor. Apart from the pyramid sensor, the sensors shall be described briefly here.

Hartmann-Shack sensor

Measurement of a wavefront with the Hartmann-Shack sensor (HSS) is carried out by a two dimensional array of micro-lenses which focuses the wavefront in the focal plane of the lenslet array in as many spots as the number of microlenses the wavefront has illuminated. According to the mean tilt $\alpha_x = \frac{\delta W}{\delta x}$ in x-direction and $\alpha_y = \frac{\delta W}{\delta y}$ in y-direction of the wavefront over the subaperture of one lens, the focused spot will be shifted by

$$\Delta x_F^i \;=\; f * \frac{\delta W}{\delta x^i}, \qquad \Delta y_F^i \;=\; f * \frac{\delta W}{\delta y^i} \tag{3.1}$$

away from the center[1] for small aberrations; i is the corresponding microlens, f the focal length of the microlens, x_F and y_F are the coordinates in the focal plane, x and y the coordinates in the plane of the lens array. W is the wavefront deviation from the plane wave and is just the eikonal S of section 2.2, denominating it here W. Thus, the spot displacement is proportional to the mean local wavefront slope and a reconstruction of the wavefront can be processed with the exception of the irrelevant piston value. For large mean tilts the exact relation $\alpha_x = \frac{\delta W}{\delta x^i} = \arctan \frac{\Delta x_F^i}{f}$ (and accordingly for the y-direction) has to be applied.
If the unexpanded beam is illuminating the lenslet array, the spacial resolution of the HSS is given by the size of the micro-lenses. Phase information

[1] the position of the spot for an unaberrated wavefront

is retrieved from the discrete values of local wavefront tilts.

Interferometric sensor

In a Twyman-Green wavefront sensor, similar to the Michelson-interferometer, one plane wavefront is divided by a beamsplitter into two. One of them is aberrated by crossing or being reflected at the optical medium to be tested. The aberrated wavefront is then superimposed with the reference plane wavefront. The resulting interference pattern depends on the phase differences of both wavefronts. Non-linear numerical calculations provide the aberrations of the deformed wavefront (see 6.2.2).

Curvature sensor

In a curvature sensor, the relation between signal and phase is a non-linear one as in the interferometric sensor. It measures the Laplacian of the wavefront distortion [Rod90]. For that purpose a perfect lens is placed in the wavefront which is being tested. The intensity profiles in two complementary planes, located at a distance d before and at the same distance after the focal plane are detected. The difference of the intensities is approximately proportional to the local wavefront curvature. But the sensor's validity is restrained to the case of a uniform intensity distribution in the plane where the phase is desired to be known [Sot03]. The phase ϕ can be calculated from

$$\nabla^2\phi(x,y)\cdot I_0 = -\left[\frac{\partial I(x,y)}{\partial z}\right]_{z=0}$$

if z is the direction of propagation. To reconstruct the wavefront, the Poisson equation must be solved.
The gain (that is the response of the sensor relative to the aberration) can be changed "on the fly" by regulating the amount of defocus which is used to retrieve the wavefront Laplacian.

Pyramid sensor

Like the curvature sensor, the pyramid sensor (PS) can also change the gain on the fly by changing the modulation amplitude. In modulation mode and for small aberrations, the response is a good linear approximation to the wavefront derivate. The resolution is given, as for the curvature sensor, by the amount of sensor pixels used which can be changed easily. Although the pyramid sensor is able to measure large aberrations it is also very sensitive to smallest aberrations.

3.1 Pyramid Sensor - The Geometrical Description

It was Ragazzoni in 1996 who proposed to use a prism with pyramidal form for wavefront sensing in astronomy [Rag96]. His idea was based on a very old method to test the focal point of a lens, the so-called Foucault knife test.

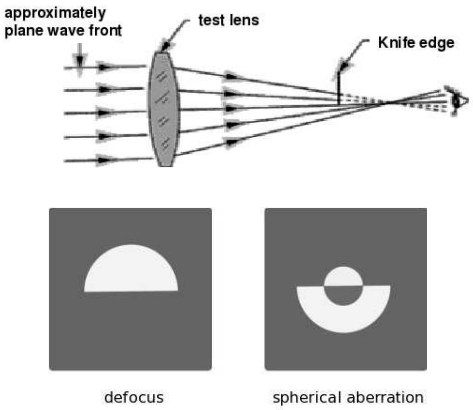

Figure 3.1: The Foucault knife test for a lens with the knife edge placed at the expected but wrong focal point (top). The bottom pictures show the illumination after the knife edge for a lens with defocus and for a lens with spherical aberration.

This test consists of illuminating the lens which is to be tested with a plane wavefront and to place a knife blade in the supposed focal plane, so that the knife edge is oriented for example horizontally and is 'touching' the optical axis (Fig. 3.1). If the real focus is more distant from the lens than the knife, the upper half of the rays is blocked resulting in an illuminated upper half circle in the plane of observation. For a lens with spherical aberrations, where the outer rays have a focal length f_o closer to the lens than the focal length f_i of the inner rays, the blade introduced at a focal distance between f_o and f_i will block the rays coming from the inner upper half and those from the outer lower half resulting in the complementary image (Fig. 3.1).

If the knife edge is replaced by a roof prism, none of the rays will be blocked, but the upper half of the rays will be separated spatially from the lower half by refraction. With such a roof prism (see Fig. 3.2) we only can get information of the aberrations in one dimension, thus a pyramid prism with at least three sides is needed to distinguish both dimensions. The pyramid can have $n \geq 3$ sides[2] to get information about the aberrations in both dimensions perpendicular to the optical axis [Cla03].
In the pyramid sensor a perfect lens with a well-known focal length focuses

[2]the so called number of "sides" always refers to the number of facets around the tip

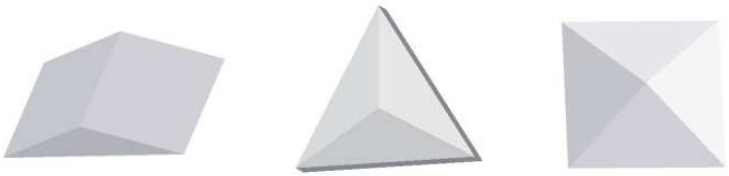

Figure 3.2: A roof prism, a 3-sided pyramid prism and a 4-sided pyramid prism.

the wavefront to be tested onto the pyramid's tip which is placed exactly at the focal point of the lens.

3.1.1 The 3-sided prism

We denote a coordinate system (x, y) at the pupil plane, that is the plane of the lens, and a coordinate system (x_f, y_f) at the focal plane of the lens, that is the plane perpendicular to the optical axis including the pyramid's tip position, with both x-coordinates horizontal, and both y-coordinates vertical, the origin being on the optical axis. A ray emitted from a point Q(x';y') in the entrance pupil that has a slope $\frac{\partial W(x',y')}{\partial x}$ and $\frac{\partial W(x',y')}{\partial y}$ in x- and y-direction respectively, will reach the point $Q_f(x'_f; y'_f)$ in the focal plane with

$$(x'_f, y'_f) = f \cdot \left(\frac{\partial W(x,y)}{\partial x}, \frac{\partial W(x,y)}{\partial y} \right) \Big|_{\substack{x=x' \\ y=y'}} . \tag{3.2}$$

A ray originating from a point in the lens pupil will either be displaced to face A_1, A_2, or A_3 of the pyramid (Fig. 3.3) depending on the signs of the

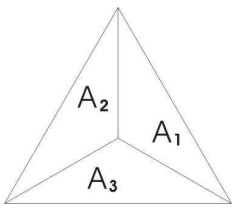

Figure 3.3: Topview on the tip of the 3-sided pyramid prism with its 3 refracting planes.

derivates $\frac{\partial W(x,y)}{\partial x}$ and $\frac{\partial W(x,y)}{\partial y}$. It will reach the corresponding pupil in the image plane as can be seen in Fig. 3.4, where the ray reaches the lower facet

according to its tilt and thus illuminates the corresponding point in image pupil P_3, while the conjugate points in image pupil P_1 and image pupil P_2 remain dark.

So far, only information about the sign of the wavefront derivation can be obtained as e.g. for a small positive defocus and a big positive defocus the image is the same. To get an quantitative information about the aberrations the pyramid can be moved circularly. This is done by moving the pyramid with its symmetry axis remaining parallel to the optical axis, letting the tip describe a circle of radius r_T (the modulation amplitude) with the frequency $\frac{1}{T}$ around the origin of the (x_f,y_f)-plane. Alternatively the beam spot can

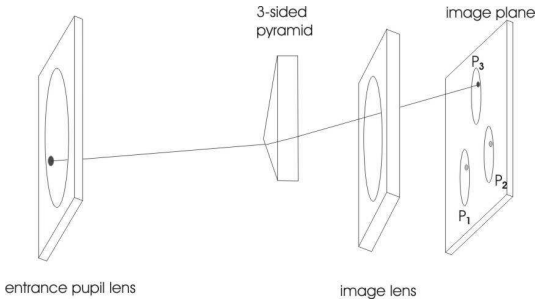

Figure 3.4: A ray from a generic point in the entrance pupil with a tilt will not be focused on the pyramid's tip but will be displaced from the focus. It will be refracted by one of the three pyramid's planes to the corresponding pupil. The vertex of the pyramid is positioned at the nominal focus point of the pupil lens.

be modulated around the fixed tip with a piezo-driven motor. Assuming that the intensities of the pupils are integrated over one period T, the intensity pattern of the pupils now depends on $\frac{\partial W(x,y)}{\partial x}$ and $\frac{\partial W(x,y)}{\partial y}$.

3.1.2 Modulation of a roof prism

To derive the signal in case of modulation, let's consider the one dimensional case with a roof prism. Assuming that the displacement of the ray from the roof edge due to a slope $\frac{\partial W(x,y)}{\partial y}$ is e.g. $f \cdot \frac{\partial W(x,y)}{\partial y} = h < 0$ (Fig. 3.5); if a sinusoidal modulation with amplitude a (corresponding to r_t for circular movement) and frequency $f = \frac{1}{T}$ of the pyramid moving parallel to the y-axis is done, the spot will remain within a time interval Δt_1 in the upper roof facet, and within a time interval $\Delta t_2 > \Delta t_1$ in the lower roof facet, with $\Delta t_1 + \Delta t_2 = T$. If the intensities of the two pixels in the two image pupils are integrated over one period the ratio between the intensity I_u and the

intensity I_L is equal to the ratio of the time the spot spends in each facet of the roof-prism, that is

$$\frac{\Delta t_2}{\Delta t_1} = \frac{I_L}{I_u}$$

if I_u is the intensity of one pixel measured in the pupil corresponding to the upper facet and I_L the intensity of the equivalent pixel in the lower pupil.

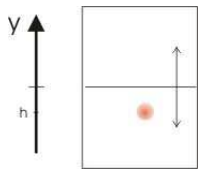

Figure 3.5: Sinusoidal modulation in one dimension of a roof prism. The beam is focused at a distance h<0 from the roof edge when the prism is in its center position.

If the blurred spot lies inside the modulation amplitude, the signal will never be saturated; that means – regarding only one dimension – that $\frac{\delta W(x,y)}{\delta y} < \frac{a}{f}$. If additionally the aberrations are small compared to the modulation amplitude the signal is approximatively linear to the wavefront derivative (right curve, Fig. 3.6), like it is the case in the HSS.

The gain of the sensor can be adapted in closed-loop. When starting closed-loop with big aberrations, the modulation amplitude has to be big enough, so that the signal is not saturated. While correcting and thus decreasing the aberrations, the amplitude is diminished and the sensor keeps in this way a high sensitivity and maintains a good signal to noise ratio.

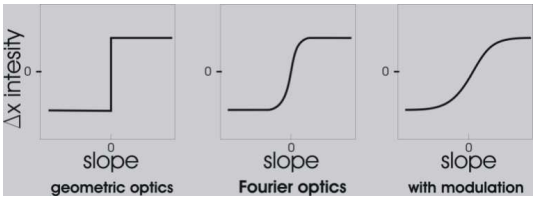

Figure 3.6: Intensity difference of conjugate pixels in the pupils, depending on the tilt (slope) of the wavefront: in geometric optics for a static pyramid (left), in Fourier optics for a static pyramid (middle) and for a modulated pyramid (right).

3.1.3 The 4-sided prism

To obtain the aberrations in x- and y-direction two roof prisms oriented perpendicularly to each other are needed or, equivalently, a 4-sided pyramid

prism is need. By defining the signals $S_x = S_x(x, y)$ and $S_y = S_y(x, y)$ for a pupil point at $x = l$ and $y = m$ in the entrance pupil as the normalized intensity differences that the corresponding pixels have in the four pupil images, we can write this relation the following way:

$$\left.\frac{\partial W}{\partial x}\right|_{l,m} \sim S_x(l,m) = \left.\frac{(I_1+I_4)-(I_2+I_3)}{I_S}\right|_{l,m}$$
$$\left.\frac{\partial W}{\partial y}\right|_{l,m} \sim S_y(l,m) = \left.\frac{(I_1+I_2)-(I_3+I_4)}{I_S}\right|_{l,m}$$

where I_n is the intensity at the corresponding pixel (l,m) of pupil $n = \{1, 2, 3, 4\}$ in the image plane; I_s is the overall intensity of that pixel in all 4 pupils. In the geometrical approximation S_x and S_y are proportional to the slopes in x and y direction respectively.

The sampling (corresponding to the spatial resolution) is given by the number of pixels on the detector (CCD-camera) that are used for each pupil. So, to enhance resolution for a given sensor, the image pupil size has to increase; this can be done easily by increasing the focal length of the image lens in Fig. 3.4 assuming that the intensity is high enough to keep a tolerable signal to noise ratio.

3.2 Edge and Tip Quality

The minimum necessary edge and tip quality is determined by the smallest spot size, i.e. the Airy-disc of a diffraction limited wavefront for a circular pupil. This means for a limiting pupil of radius r_p and wavelength λ and lens of focal length f a spot size of radius

$$r_{Airy} = 1.22\frac{f \cdot \lambda}{2 \cdot r_p}. \tag{3.3}$$

To get a quantitative value we anticipate here the parameters mentioned in chapter 6.3; we get, for our wavelength, our focal length and our entrance pupil, a diffraction limited spot of radius $r_{Airy} = 80\mu m$.
If a loss of 20% caused by scattering of light at the turned edges of the pyramid is tolerated, the width of the edges has to be $<18\mu m$. For a loss of less than 10% on the edges the width has to be $<9\mu m$ wide. Producing pyramids with such sharp edges and such flat facet angles[3] is very difficult, especially taking into account that a further demand is that the facets should be as plane as possible near the tip (that is at distances around the tip, where the wavefront is focused) and at the pyramid's base, where the beam(s) are

[3] around 3° are used in astronomy reaching a roof length of $9\mu m$ and turned edges of $9.2\mu m$ [Rag00]

transmitted. The pyramids used at the moment in AO systems are 4-sided pyramids. They have two additional inherent problems compared to 3-sided pyramids. First, for an edge production of the same quality, i.e. the same width as for the 3-sided pyramid, the amount of scattered light is (at least) 33% higher for the 4-sided just because of the additional edge. The second disadvantage is that while polishing not a tip but usually a roof is created. Consequently the area able to scatter light increases and the geometrical symmetry is not given anymore. When polishing the last (two) side(s) it is very difficult to avoid a roof, which happens when the lapping is stopped too early or too late. Further, for flat pyramids the polishing agent can pass on to already good polished faces, deteriorating them. When polishing a 3-sided prism no lapping problems arise.

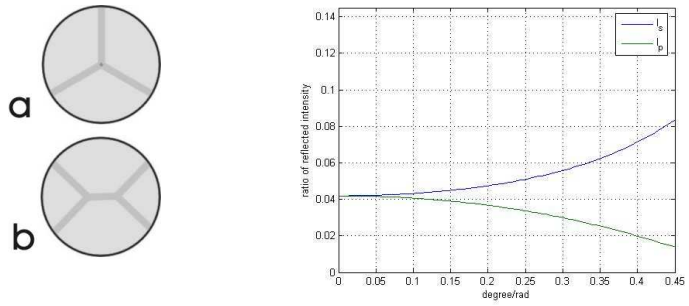

Figure 3.7: Signal loss when focusing on the pyramid's tip. The cause is imperfect, finite edge and tip size of the 3-sided (a) and the 4-sided (b) pyramid and loss of light by reflection (right).

Additional signal loss is due to the reflected light on all surfaces. Anti-reflection coatings that are used for other optics like lenses are avoided here as the coating distribution on edges is critical and not as homogeneous as it can be manufactured when having continuous, smooth surfaces.
A few years ago a group in Basovizza-Trieste, Italy, manufactured a pyramid prism of plexiglass by means of deep x-ray lithography [Ghi03]. The quality achieved with this method is easier to reproduce than with the 'hand made', polished prisms. The prism that they produced had a vertex angle of 178.3°(that is a facet angle of less than 1°) and turned edges of 35μm which is not as good as the turned edges achieved with polishing.

Fresnel equations quantify the amount of light that is reflected in dependence of the polarization of the light. As can be seen in Fig. 3.7, for small angles of incidence – as it is the case for the flat pyramid used – the transparency is nearly the same for both polarizations. The curves are calcu-

lated with $n = 1.513$ representing the refraction index of BK7 glass for both wavelengths used in this work ($n_{632} = 1.5151$, $n_{783} = 1.5111$ [Mel06]). If the facets' slope is too big, it will not only be difficult to capture the image pupils with one sensor, but the signal attenuation through the pyramid will depend on the polarization.

3.3 Beam Splitting by the 3-sided Pyramid

The splitting of the focused beam on the 3-sided pyramid happens at geometrically symmetric facets A_1, A_2, and A_3. Mathematically we denote this as transmission functions K_1, K_2, and K_3 for each facet, with transmission 1 in the corresponding facet area and 0 outside.

$$K_1(x,y) = \begin{cases} 1; & x > 0 \wedge y > \frac{-1}{\sqrt{3}} \cdot x; \\ 0; & else \end{cases}$$

$$K_2(x,y) = \begin{cases} 1; & x < 0 \wedge y > \frac{1}{\sqrt{3}} \cdot x; \\ 0; & else \end{cases}$$

$$K_3(x,y) = \begin{cases} 1; & (x < 0 \wedge y < \frac{1}{\sqrt{3}} \cdot x) \wedge (x > 0 \wedge y < \frac{-1}{\sqrt{3}} \cdot x); \\ 0; & else \end{cases}$$

The 3-sided pyramid thus splits the incoming beam into three beams. The centre of these three beams has a deviation angle γ'' from the optical axis in three opposed directions, the so called splitting angle. γ'' depends on the angle between the facets. The deviation angle from the optical axis is, applying Snell's refraction law, derived as

$$sin\gamma'' = n \cdot \sin(\gamma - \arcsin(\sin\gamma \cdot \frac{1}{n})) \tag{3.4}$$

with γ being the angle of a pyramid facet relative to its base, which is equal to the incidence angle of the center of the wavefront. For small γ this can be simplified to

$$\gamma'' \quad = \quad \gamma(n-1)\,.$$

If r_p is the distance of the pupils' center to the optical axis, the distance d_p between two of the three pupils will be $d_p = r_p\sqrt{3}$. So at a distance D from the vertex of the pyramid the distance between the pupils is $d_p \approx \sqrt{3}D{\cdot}tan\gamma''$. The approximation holds, as long as we can neglect the parallel shift inside the pyramid.

3.4 Diffractive Description of the Pyramid Sensor

The description in terms of geometrical optics depicts the basic idea of how the PS works so it is understood intuitively. This geometrical approximation can be used very well to describe the PS in modulation operation. However, it is clear, that as soon as we deal with a static pyramid where the beam is focused on the tip, diffraction can no longer be neglected.

The pyramid's facets can be seen as 3 spacial filters, the tilt of the pyramid's facets only serving for separating the 3 images in space. When the wavefront's aberrations are quite small, the beam will be focused to a small spot too, the interference and diffraction effects then playing an important role. In the following, the relation between the electric field in the pupil image plane and the electric field in the entrance pupil is derived.

Let the entrance pupil be defined by the opening of the perfect lens of focal length f and of radius 1. We name the coordinates of the plane of the entrance pupil (x, y) as in section 3.1.1. At a distance of one focal length, we have the focal (or Fourier) plane (x_f, y_f), and at one additional focal length we nominate the image plane with (x_i, y_i).
Fraunhofer diffraction describes the electric field distribution in an image plane at infinity after diffraction of a wavefront on an aperture. With a lens this image can be brought to a finite distance, that is, to the focal plane.
It can be shown [Goo05] that - apart from a constant factor - the electric field $A_f(x_f, y_f)$ in the focal plane is the Fourier transformation $\mathcal{F}$ of the electric field $A(x, y)$ of wavelength λ in the aperture plane,

$$\begin{aligned} A_f(x_f, y_f) &= \int\int_{-\infty}^{+\infty} A(x,y) exp\left[-i\frac{2\pi}{f\cdot\lambda}(x_f x + y_f y)\right] dx\, dy \\ A_f(\tilde{x}_f, \tilde{y}_f) &= \int\int_{-\infty}^{+\infty} A(x,y) exp\left[-i2\pi(\tilde{x}_f x + \tilde{y}_f y)\right] dx\, dy \\ &= \mathcal{F}\{A(x,y)\} \end{aligned} \tag{3.5}$$

replacing x_f and y_f by the spatial frequencies $\tilde{x}_f = \frac{x_f}{f\cdot\lambda}$ and $\tilde{y}_f = \frac{y_f}{f\cdot\lambda}$ in the second line. If no optical component is placed at the focal plane the wavefronts will propagate to the image plane, where the electric field $A_i(x_i, y_i)$ is the inverse Fourier transformation $\mathcal{F}^{-1}$ of the electric field $A_f(\tilde{x}_f, \tilde{y}_f)$ in the focal plane:

$$\begin{aligned} A_i(x_i, y_i) &= \mathcal{F}^{-1}\{A_f(\tilde{x}_f, \tilde{y}_f)\} \\ &= \int\int_{-\infty}^{+\infty} A_f(\tilde{x}_f, \tilde{y}_f) exp\left[+i2\pi(\tilde{x}_f x_i + \tilde{y}_f y_i)\right] d\tilde{x}_f\, d\tilde{y}_f \end{aligned}$$

If the 3-sided pyramid is placed at the focal plane, it acts as a spatial filter there. To calculate the electric field distribution in image pupil P_1 we can think of the pyramid as a transmission filter with transmission 1 in the area of facet A_1 and transmission 0 for the remaining areas A_2 and A_3 as in section 3.3, but adding a phase term to take into account the tilts of the facets. Further x is renamed to $\tilde{x}_f$ and y to $\tilde{y}_f$ as the "filter" is located in the focal plane. Grouping to one single transmission function K and re-expressing the domain, we can write

$$K(\tilde{x}_f, \tilde{y}_f) = \begin{cases} e^{i2\pi s(-\sqrt{3}\tilde{x}_f + 3\tilde{y}_f)} & -\frac{\pi}{6} < arctan(\frac{\tilde{y}_f}{\tilde{x}_f}) < \frac{\pi}{2} \\ e^{i2\pi s(\sqrt{3}\tilde{x}_f + 3\tilde{y}_f)} & \frac{\pi}{2} < arctan(\frac{\tilde{y}_f}{\tilde{x}_f}) < \frac{7\pi}{6} \\ e^{i2\pi s(6\tilde{y}_f)} & \frac{7\pi}{6} < arctan(\frac{\tilde{y}_f}{\tilde{x}_f}) < \frac{11\pi}{6} \end{cases}$$

where s is the slope of the facets and the term in brackets after s is the projected distance for a point on each facet to the tip, i.e. the distance between the tip and the point's projection onto the centre line of the corresponding facet.

The electric field in the image plane is thus given by the inverse Fourier transformation of the field in the focal plane multiplied with the filter function $K(\tilde{x}_f, \tilde{y}_f)$. We then get the following expression describing the field in the image pupil:

$$\begin{aligned} A_i(x_i, y_i) &= \mathcal{F}^{-1}\{K(\tilde{x}_f, \tilde{y}_f) \cdot A_f(\tilde{x}_f, \tilde{y}_f)\} \\ &= \int\int_{-\infty}^{+\infty} \left[K(\tilde{x}_f, \tilde{y}_f) \cdot A_f(\tilde{x}_f, \tilde{y}_f) \cdot e^{+i2\pi(\tilde{x}_f x_i + \tilde{y}_f y_i)}\right] d\tilde{x}_f \, d\tilde{y}_f \\ &= \mathcal{F}^{-1}\{K(\tilde{x}_f, \tilde{y}_f) \cdot \mathcal{F}\{A(x, y)\}\} \end{aligned} \tag{3.6}$$

Using the convolution theorem

$$\begin{aligned} \mathcal{F}\{a \odot b\} &= \mathcal{F}\{a\} \cdot \mathcal{F}\{b\} \\ = A \cdot B &= \mathcal{F}\{\mathcal{F}^{-1}\{A\} \odot \mathcal{F}^{-1}\{B\}\} \end{aligned}$$

we can rewrite Eq.(3.6) to

$$A_i(x_i, y_i) = \mathcal{F}^{-1}\left\{\mathcal{F}\{k(x, y)\} \cdot \mathcal{F}\{A(x, y)\}\right\}. \tag{3.7}$$

As the convolution and the Fourier operator are linear operators we can simplify this to

$$A_i(x_i, y_i) = k(x_i, y_i) \odot A(x_i, y_i) \tag{3.8}$$

if k is the inverse Fourier transformation of K, $k(x_i, y_i) = \mathcal{F}^{-1}\{K(\tilde{x}_f, \tilde{y}_f)\}$. So, the electric field of the pupil images is given by the convolution of the

inverse Fourier transform of the filter function with the electric field in the entrance pupil.

Chapter 4

Active Elements

Two different actuators are commonly used to correct the aberrated wavefront in adaptive optics: liquid crystal transmission plates or deformable mirrors.

Liquid crystal modulators alter polarized light passing through them with a change of phase and amplitude. This technique has the disadvantage of being only capable of a slow bandwidth comprising only a few Hertz. But investigation is being done in this field [Pis06] and regarding the high production quantities in the area of liquid crystal displays, it is probable that fast and cheap crystal modulators will be available soon.

Deformable mirrors act independently of the light's polarization and are faster than the liquid crystal modulators. In this work a membrane mirror is used as actuator in the optical set-up. In addition, also a segmented mirror was tested.

4.1 Membrane Mirror

The deformable mirror consists of 37 hexagonal pistons lying under a silicon-nitride membrane coated with aluminium. The membrane is stretched over a frame with a round opening. Its deformation is caused by electrostatic forces between the pistons and the membrane. The deformation is not linear to the applied voltage between piston and membrane, but exhibits in good approximation a quadratic dependence.
The electrostatic force F is given by

$$F = \varepsilon \frac{A}{d^2} V^2. \tag{4.1}$$

A is the area over each piston, V is the voltage between a piston and the membrane, d the distance between membrane and piston, and $\varepsilon = \varepsilon_r \varepsilon_0$ is

the permittivity.
If a bias voltage V_b is applied and a much smaller control voltage V_c is added to it, so that $V_c \ll V_b$, then the sensitivity $\frac{F}{V_c}$ of the mirror becomes linear:

$$F = \varepsilon \frac{A}{d^2}(V_b + V_c)^2 \quad \Leftrightarrow \quad \frac{F}{V_c} \approx 2\varepsilon \frac{A}{d^2} V_b \tag{4.2}$$

Complexity comes from the fact that the pistons are not independent, i.e. putting a voltage on one piston moves the membrane over it but also over the surrounding pistons (cross-talk). This is expressed mathematically by the Poisson equation

$$\triangle D = -\frac{\rho}{T}$$

where D is the deflection of the membrane, $\rho = F/A$ is the load and T is the tension of the membrane which is assumed to be constant. The load depends on the distance d, which itself depends on the applied force: $\rho = \varepsilon V^2/d(\rho)$. The boundary condition is given by the circular opening of the wafer.

The Poisson equation, describing the shape of the mirror, must be evaluated under the condition $D_c(x_c, y_c) = 0$, i.e. no deflection of the membrane where it is fixed to the wafer at its contour (x_c, y_c) [VdoS95].

The order of magnitude of d is around $100\mu m$ with a deflection of a few μm (see chapter 6.1.1).

4.2 Segmented Mirror

The deformation of a micro-electromechanical system (MEMS) mirror is done via electrostatic forces like in case of the membrane mirror. The MEMS mirror consists of an array of many very small segmented mirrors (pixel mirrors). It is fabricated using modified silicon technology production processes of the integrated circuit industry. Photolithography is used making the production very precise, producing devices of μm-size and reducing the costs per unit, as huge fabrication amounts can be produced nearly at the same expenses as smaller amounts.

The pixel mirrors have a squared shape and are connected to the substrate by four thin legs, so a small force is needed to sink each mirror. The behaviour of a pixel mirror depends amongst other things on the thickness δ of the squared pixel plate, the distance h between the plate and the substrate, and the width d of a square. For a same deformation amplitude, a smaller voltage has to be applied between the plate and the electrode on top of the substrate, the bigger d and the smaller h and δ are.

Chapter 5

Neural Networks for the Pyramid Sensor

Compared to the geometrical regime, the diffractive regime of the pyramid sensor is mathematically more complex, especially not being linear in its behavior. Smallest alignment errors cause big signal changes in this sensitive region. So the idea of using an alternative controller emerged: to use an individual neural network that perfectly fits the special set-up instead of an approximated analytical calculation frame. Artificial neural networks can learn and realize control algorithms which are mathematically difficult or which cannot be derived analytically. Thus, assuming that a control algorithm exists, a net can be built, letting the net generate the appropriate control algorithm during network training.

Although neural networks have been developed for more than 4 decades, it is still a fuzzy tool in the sense that there is no exact "recipe" for what the neural network (NN) should look like for a given problem. For specific problem types, like for example, face recognition, function approximation, classification, and the like, a rough NN structure is recommended. But the subtle details of the net, which make it the best fitting net for the specific task, have to be improved step by step with "the experimentor's experience".

For an introductory explanation a neural network can be seen as a black box having an input and an output: the input being for example an array or vector of size n, and the output a vector of size m. Imagine the black box being an unknown function f: $\Re^n \rightarrow \Re^m$ with a multitude of adjustable parameters, the so-called weights. Now the weights should have those values, that – for all given input-output-pairs of a problem – f will map the input vector onto the output vector. For the given task that the network shall

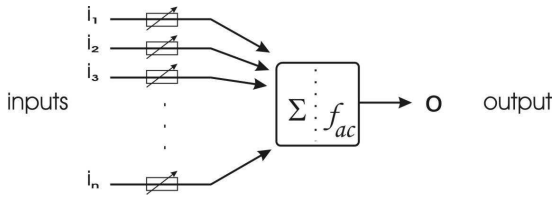

Figure 5.1: Basic unit of a neural network

represent, many pairs are required; the more complex the problem, the more examples have to be available. This is similar to the case of doing regression of a data set. The search of the adequate weights is called training or learning.

Instead of an input vector we have a two dimensional matrix as input: the image of the 3 pupils. Our output vector is the wavefront aberration, coded as the height levels of the mirror pistons. Therefore f maps $(\Re^n \times \Re^n) \rightarrow \Re^m$ with $n \times n$ being the number of pixels of the pupils image and m the number of pistons producing the aberration for compensation.

5.1 Structure of a Neural Network

A neural network is composed of many units, also called nodes or neurons, which are connected by links. A number, the weight, is associated with each link.
Neurons in an artificial neural network are usually structured in layers. The network sketched in Fig. 5.2 as an example, consists of 4 layers: the input layer (although this is a layer without calculating nodes as will be seen later) with four inputs, the first neuron layer with 3 neurons, the second layer with 4 and the last layer, the output layer, with two neurons.

In a fully connected network each neuron of one layer is connected to all neurons of the layer before (layer on the left side) and to all neurons of the layer afterwards (layer on the right side) via links. The notation of a link's weight w_{ij}^l stands for the weight to neuron i of layer number l from the j-th neuron of the previous layer. The output value of a neuron is obtained from a simple computation depending on the input values and the weight values. Each input to a neuron (usually the outputs of the neurons of the previous layer) is multiplied with the weight of the link it is passing through (Fig.5.1). These assessed inputs are summed up in the neuron, adding optionally a bias b; the sum is used as new input for the activation function f_{ac}. The activation function is a nonlinear function that calculates the neuron's output value from the weighted sum. Typical activation functions are the sign function,

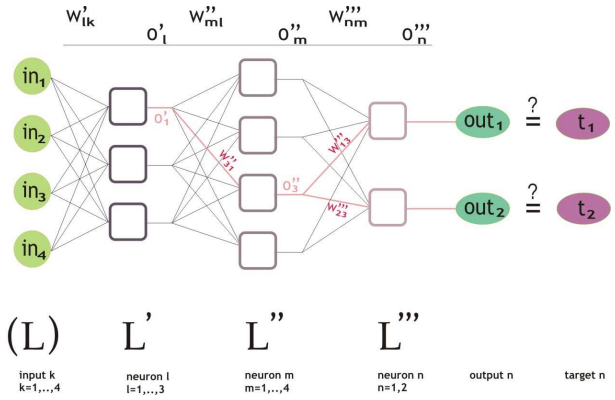

Figure 5.2: Adjustment of the weight coefficients in a fully connected network with 4 layers, 4 input values and two output values.

the sigmoid function or the hyperbolic tangent function.

$$sign(x) = \begin{cases} +1, & x \geq 0 \\ -1, & x < 0 \end{cases} \quad ; \quad sigmoid(x) = \frac{1}{1+e^{-x}}; \quad tanh(x) = \frac{e^{2x}-1}{e^{2x}+1}$$

The activation function can be in principle any function that is monotone, continuously differentiable (the sign function being an obvious exception), with a finite range. Usually all nodes of the network have the same activation function.
The calculation of the output values from the input values is executed straight forward from layers on the left to the right. Networks with more than two layers are called asynchronous networks because the activation of the neurons of one layer is processed parallel (that is synchronous), but beginning with the first layer on the left and following layer by layer to the right.
The outputs out_1 and out_2 in Fig. 5.2 are calculated as follows:

To refer to the different values of the net, it is convenient to represent all inputs by an input vector $\overrightarrow{in}$, the outputs by an output vector $\overrightarrow{out}$ and the weights of the links connecting layer $(l-1)$ and layer l by the weight matrix W'. W' is of size $(t \times s)$ if s is the number of neurons in layer $(l-1)$ and t the number of neurons in layer l. We now can describe the output of the net above by:

$$\overrightarrow{out} = \overrightarrow{o'''} = f_{ac}(W''' \cdot f_{ac}(W'' \cdot f_{ac}(W'\overrightarrow{in})))$$

Building a neural network requires a decision on which form the net should have, that is, how many layers the net should have, how many units each

layer should have and how they should be connected with each other.
In the example above the net is linked unidirectionally. This means, outputs from one layer are connected only with layers to their right. Such networks are called feed-forward networks. If on the contrary an output of a layer serves as input of a neuron of the same layer or of any layer before it, forming a cycle, the net is called recurrent.
The layers L' and L" in Fig. 5.2 are called hidden layers as they have no direct connection to the "outside world", the inputs and the outputs, but are connected indirectly over weights to them. A single hidden layer in a network is enough to represent any continuous function, providing that there is a sufficiently large number of nodes in the hidden layer. To represent discontinuous functions two hidden layers are necessary [Rus95].

The challenge of finding an optimum network is not to take too small a net, as it will not be able to represent the task, and not to take too big a net, as it will represent the given examples very well but will tend to overfit and thus perform poorly for inputs not presented for training. This is explained in the next chapter in detail.

5.2 Training Methods

Training or learning means adjusting the weights so that the neural network represents the given task. For that, the weights are changed in such a way, that the net's output $\overrightarrow{out}_i$ for a given input $\overrightarrow{in}_i$ matches the real must output $\overrightarrow{t}_i$, also called target; If our training set consists of N input-output (must-outputs) examples, then $i = 1, 2, ..., N$.
Once the structure of the net is defined, the weights are initialized and afterwards adjusted by a learning algorithm using the input-output examples of the given task.

One of the most popular learning types is gradient descent learning, where an error or cost function $E(\overrightarrow{w})$ is defined, relating the error $\overrightarrow{\delta}_i = \overrightarrow{t}_i - \overrightarrow{out}_i$ to the weights.

5.2.1 Minimizing the error function

The simplest and most frequently used cost function is given by

$$\begin{aligned} E(\overrightarrow{w}) &= \frac{1}{2}\sum_i |\delta_i|^2 \\ &= \frac{1}{2}\sum_i \left|\overrightarrow{t}_i - \overrightarrow{out}_i(\overrightarrow{w})\right|^2 . \end{aligned} \tag{5.1}$$

Other cost functions are possible. They should be differentiable functions of δ with a minimum at $\delta = 0$. In the gradient descend algorithm the weights are changed by $\overrightarrow{\triangle w}_i$, where $\overrightarrow{\triangle w}_i$ is proportional to the error function,

$$\triangle w_{ij} = -\eta \frac{\partial E}{\partial w_{ij}} \tag{5.2}$$

$$w_{ij\,new} = w_{ij\,old} + \triangle w_{ij} \tag{5.3}$$

with the proportional factor η, called the training rate, and w_{ij} being one component of $\overrightarrow{\triangle w}_i$. For one example of the set, and for z being the number of weights (of the last layer for instance) this is the gradient at the point $\overrightarrow{\triangle w}$ of the error plane in the $(z+1)$-dimensional space. Searching for the minimum of $E(\vec{w})$ is done by sliding down the E-plane. If the chosen η is too large, the "correction" lets $\vec{w}$ jump from one side of the valley of the E-plane to the other; this happens for minima in valleys with contour lines of cigar form: because of the derivation in steep gorges the point will jump from one side of the gorge to the other, oscillating instead of gliding down. Thus, approximation to the minimum goes in a zic-zac path, or, for a too big[1] training rate η, the weight vector will even move further away from the minimum. Choosing a very small learning rate is secure, but makes training very slow.
To deal with this problem Eq. (5.2) can be modified by adding a momentum μ.

$$\triangle w_{ij} = -\eta \frac{\partial E}{\partial w_{ij}} + \mu \triangle w_{ij\,old} \tag{5.4}$$

with $0 < \mu < 1$, taking so into account the correction of the last update $\triangle w_{ij\,old}$. In this way a zic-zac path is smoothed out.

Updating the weights can be done in two modes: either by presenting all input-output examples at once or by presenting subsets to the net and then calculating the error. The former is called batch mode; doing presentation pattern-by-pattern is called incremental mode. Each run in which the net is presented a (sub)set of examples and new weights are calculated, is called an epoch.

The description above is for an update of the weights of one layer, of the last layer. So we rewrite w_{ij} in Eq. (5.2) to w'''_{nm}, where the index is now not the pattern but just the weight we are looking at. Ignoring a momentum

[1] The training rate is 'too big' if the gradient multiplied with the training rate is bigger than the width of the valley in the (projected) direction of the gradient.

and using the activation function f_{ac} we can write:

$$\begin{aligned} \triangle w'''_{ij} &= -\eta \frac{\partial E}{\partial w'''_{ij}} \\ &= -\eta \frac{\partial(\frac{1}{2}\sum_n (o'''_n - t_n))}{\partial w'''_{ij}} \end{aligned} \tag{5.5}$$

We will simplify the net above, assuming it to have one hidden layer less, letting the outputs o'_l correspond to the training inputs without loss of generalization. The dependence of the outputs o'''_n from the inputs $in'_l = o'_l$ is given by

$$\begin{aligned} o'''_n &= f_{ac}(\sum_m w'''_{nm} o''_m) \\ &= f_{ac}(\sum_m w'''_{nm} f_{ac}(\sum_l w''_{ml} in'_l)) \end{aligned} \tag{5.6}$$

Thus a weight in the (now) first hidden layer can be calculated using Eq.(5.6) via:

$$\triangle w'''_{ij} = -\eta \frac{\partial E}{\partial o''_m} \cdot \frac{\partial o''_m}{\partial in'_l} \tag{5.7}$$

In order to correct the weights of a layer, first the weights of all layers to its right have to be calculated.
This algorithm for training a network is called back-propagation, because the weights are corrected in the inverse direction as the direction in which the calculation of the outputs from the input values is done. It is the most frequently used algorithm. Many applied algorithms are just modifications of it dealing with, for instance, the problem of local minima, plateaus, or improving the speed of the training.

In a local minimum of the error function the weight vector can get stuck, it will thus slow down training or it will even prevent the ability to find the real minimum. One way to avoid or to get out of a minimum is to add a small random value to the weights. Again, a compromise has to be made, as adding too much "noise" will deteriorate the training.

5.2.2 Conjugate gradient descent

A similar training algorithm is the conjugate gradient algorithm. Instead of moving along the negative direction of the gradient, the direction of the gradient of the preceding update is also taken into account.
Consider the error function as a plane in the multidimensional space spanned

by the weights (more precisely: the weight vectors). A point at the error plane corresponds to one set of weights $\overrightarrow{w}$. Let $\overrightarrow{g}$ be the gradient vector of the plane at the point $\overrightarrow{w}$. So the direction $\overrightarrow{d}_0 = -\overrightarrow{g}_0$, where the weights $\overrightarrow{w}=\overrightarrow{w}_0$ are corrected to,is given by $\overrightarrow{w}_1 = \overrightarrow{w}_0 + \eta \overrightarrow{d}_0$ for the first update, i.e. the first time the weights are modified. The conjugate gradient algorithm modifies $\overrightarrow{d}$ for all following updates like:

$$\overrightarrow{d}_q = \alpha_q \overrightarrow{d}_{q-1} - \overrightarrow{g}_q$$

where q is the actual, $q-1$ the previous update and α_q is a factor that takes into account the difference between the previous and the present gradient. One implementation for α_q is

$$\alpha_q = \frac{\left|\overrightarrow{g}_q\right|^2}{\left|\overrightarrow{g}_{q-1}\right|^2} \quad .$$

After the first upgrade all directions of correction consider previous gradients. If the difference is too big, it seems more convenient not to consider the previous gradient, as it would slow down the gradient descent. This is done by reseting $\overrightarrow{d}$ to the negative gradient. One condition which decides when training has reached a reset point, is given by the Beale-Powell restart test. If the condition

$$\left|\overrightarrow{g}_q - \overrightarrow{g}_{q-1}\right| \geq 0.2\left|\overrightarrow{g}_q\right|^2$$

is satisfied, $\overrightarrow{d}$ is set to equal $-\overrightarrow{g}$.

The weights of the node connections are expected to be adjusted after training in such a way, that they provide the best overlapping of the calculated control vectors with the applied ones from the measured input vector or matrix. If the network is successfully trained, it is expected to predict the output values for input values not presented to training.

It is possible, that a net has achieved a very good, small error after a lot of epochs of training, but behaves very poorly when untrained data is presented to the input. This is most probably the case for an overfitted net. It happens either because the training set is too small or the net is too simple. It can be compared to a curve fitting with a small number of representations, where the fitted curve matches perfectly with the given points but does not represent the real problem. Testing the net with examples that the net has not been trained with is the crucial assessment of how well the net has actually been trained.

It should be mentioned that apart from training a net by modifying the weights, there are also more complex models, trying to copy the behaviour of biological neural cells. Deleting or creating new links and changing the activation function are some examples of possible additional features. However, this is beyond the scope of this work.

5.3 Image Pre-processing

Feeding the feed-forward, back-propagation net for training with complex images would enormously complicate the training and slow it down. A pre-processing of the images which extracts characteristic features out of them can be applied, in most cases minimizing the input number for the back-propagation net. Any a-priori information about some characteristic of the image features, especially about the contour, must be taken into account at the designing stage of the NN as it will improve the speed of the training immensely as well as the reproduction of the outputs even with noise.

5.3.1 Convolutional processing

This pre-processing is done by kernel convolution techniques and by auto encoding training.

Convolution techniques include kernels, like the simple average kernels or the border kernels, the same way as they are used for image processing [Jae97]. A kernel is a matrix of size $k \times k$, that runs over the 2-dimensional images, with matrix values that correspond to the feature which shall be filtered. The output is the convolution of the image pixel values with the kernel values. In some way it is similar to the assessed inputs for the training of the net, except that all values of one kernel are used for each pixel of the corresponding sublayer. The number of sublayers (also called planes or maps) in a hidden layer is given by the number of used features (kernels). From the two sublayers of Fig. 5.3 to the first hidden layer there are three kernels used, obtaining the three planes of the hidden layer.

5.3.2 Unsupervised Learning

A totally different way to train a net, is unsupervised learning by self-organizing of the net. Totally different to supervised backpropagation learning, here no comparison of the output with any target is done. The network must recognize, with the help of different algorithms to distinguish features or categories of, or correlations between the input patterns. The learning rule

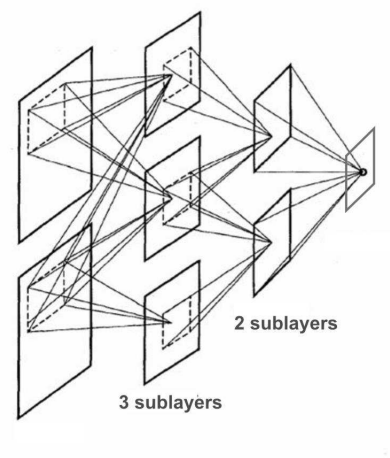

Figure 5.3: Sublayers in the feature extraction network for the pre-processing of the input image

can enforce weights, so that patterns which appear often, are supported. Alternatively the learning rule can change the network's weights in a way that it supports correlations between features of the example patterns.
Depending on what the output shall look like, different learning rules are adequate: For deeper insight to the variety of possible learning rules consult e.g. [ScE].

A special case of unsupervised learning is auto-encoding. Here the weights of the net are changed in such a way, that the output is the same as the input (or the same in the sense of its information content). In that way the trained net will map the input to the output if the input is the same or quite similar to one of the presented examples for training. This rather curious appearing mapping of the inputs to themselves is a particular way to assort the input set to groups.

Chapter 6

Laboratory Set-up

The first experimental set-up included all three sensors: the pyramid sensor, the Hartmann-Shack sensor, and the commercial Twyman-Green interferometer, using the integrated HeNe-laser of the interferometer as the light source. For the neural network training, the pyramid sensor was used without the other two sensors. Thus, all optical parameters could be changed easily without affecting the other sensors.

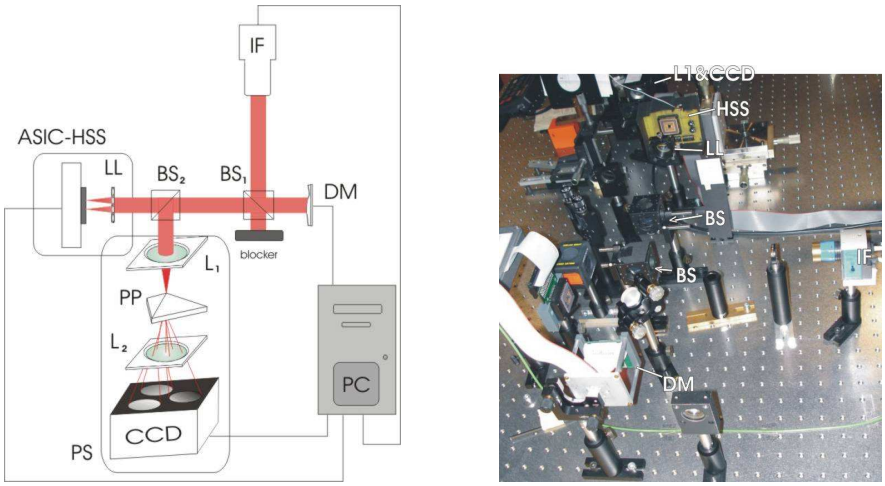

Figure 6.1: Parallel set-up of the 3 wavefront sensors: the Hartman-Shack-sensor (ASIC-HSS), the pyramid sensor (PS) and the interferometer (IF).

In the parallel set-up (Fig. 6.1), the light source of the interferometer served as a source for plane wavefronts. A beamsplitter (BS_1) reflects the beam to the deformable mirror (DM) where the wavefront suffers a phase shift of twice the deformation amplitude of the mirror. On its way back the aberrated beam is split at BS_1. One part of the beam returns to the

interferometer and the other is split at the second beam splitter BS_2. The transmitted beam passes the lenslet array (LL) and reaches the detection ASIC-chip of the Hartman-Shack sensor. The reflected beam passes the entrance pupil lens 1 (L_1) which focuses the beam onto the tip of the pyramid prism (PP). The prism separates the focused spot in the Fourier plane into three beams. After passing the imaging lens L_2 a CCD camera records the image of the entrance pupil in the conjugate plane. The interferometer, the lens L_1 and the lenslet array are all placed at a distance D away from the deformable mirror. This is done to avoid three 4f-setups – for each sensor one – with which a wavefront measurement conjugate to the plane of the DM would be realized; thus, the wavefront aberrations measured are those of the wavefront at a distance D away from the mirror.

In the set-up which is used to train the neural network for the pyramid sensor, the plane wavefront is supplied by a superluminescence diode. The beam is reflected under a small angle on the deformable mirror, restricting a bit the effective stroke range of the mirror but avoiding a beam splitter in this way (see Fig. 7.11). The aberrated beam is reflected on a mirror, which serves only for the purpose of easier aligning, and then passes the entrance pupil, which is given by the mounting of the lens L_1. The beam is split again in the focal plane by the pyramid into three beams. These three beams are reflected at 3 mirrors, so that their directions are not diverging any more, before passing through the imaging lens to the CCD camera.

In the following the optical and the electrical components of the set-up are described in more detail.

6.1 Deformable Mirror

Two mirrors were available as active elements: a membrane mirror and a recently delivered segment mirror.

6.1.1 OKO membrane mirror

The deformable membrane mirror (DM_m) from OKO Technologies in Delft, Netherlands, with its 37 pistons (segments) has a diameter of 15mm, the pistons forming an active area of 12mm diameter (Fig. 6.2).
When it is in a neutral position, that is when no voltage is applied, the membrane shows an intrinsic astigmatism of $<0.6\mu m$ (peak value). This is explained by a membrane attached inhomogeneously to the frame. Maximum deflection according to the manufacturer is achieced under a load of

255V [1]. This was controlled in our group [Wue99] with an interferometer. The quadratic relation between control voltage and deflection was confirmed and the deflection when applying 255V reached $1.1\mu m$. The cross-talk relation was confirmed too; the bigger the difference of the voltages on two neighbouring pistons, the bigger the cross-talk effect. Aggravation of the mirrors behaviour or flexibility was measured four years later [Kie03] when the peak-to-value deflection had decreased by more than 10% to under $1\mu m$. Therefore we repeated this measurement (Sec. 7.3.2).

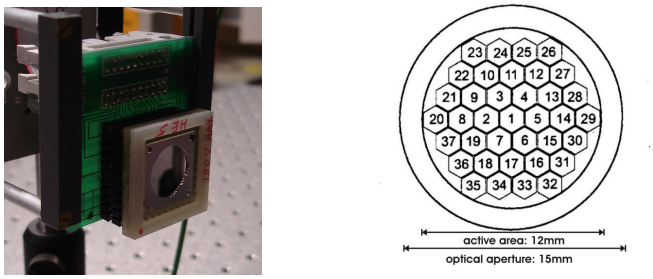

Figure 6.2: Photo of the membrane mirror (left) and a sketch of the piston arrangement under the membrane (right).

The electrostatic control of the deflection of the mirror membrane is only possible unidirectionally, towards the pistons.

Not all 37 but only the inner 19 pistons of our mirror were addressed.

Amplifier for membrane mirror

In order to address the 19 inner mirror pistons plus the membrane, with voltages between a piston and the membrane being up to 225V (staying in that way around 12% below the recommended maximum voltage), an amplifier is used as intermediary between the computer and the mirror. As the computer has an output voltage range of $\pm 5V$, amplification by a factor of 50 is necessary. The power supply for the amplifier is a Rohde&Schwarz device providing a quite stabilized and low-noise output.

D/A converter

The interface between computer and amplifier is a digital-analog converter with 4×20 channels and a bandwidth of 770Hz. Twenty channels are used to address the 19 pistons plus membrane of the OKO mirror. The channel's

[1] but it is recommendable to keep the applied voltage quite below it, to maintain a durable membrane with unchanged elasticity

output range used is 0V to +5V. The converter card is an ISA bus card restricting its use to only relatively old computer mainboards.
For the MEMS mirror 2×20 channels of this card are used.

6.1.2 MEMS mirror

Our MEMS deformable mirror (DM_s) was developed in the Fraunhofer Institute for Photonic Microsystems in Dresden.

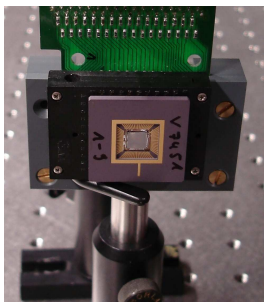

Figure 6.3: Photo of MEMS mirror

The mirror consists of 8×8 squared pixel groups, that can be addressed independently. 15×15 pixel mirror elements form one pixel group. Each mirror element is $15\mu m \times 15\mu m$ in size, so that the size of one controllable pixel group is $600\mu m \times 600\mu m$. The quadratic relation between the applied

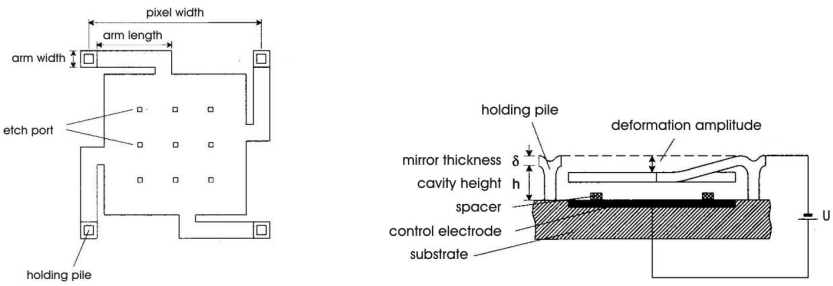

Figure 6.4: Topview of one pixel of the MEMS mirror (left) and side view (right picture) [FIP05].

voltage and the deflection of one pixel (group) can be seen in Fig. 6.5 . The relation can be approximated very well by $z = \frac{37}{90}U^2$, where z is the deflection (in nm) and U is the Voltage. By applying a maximum voltage of only $<35V$ the maximum deflection of $400nm$ is reached.

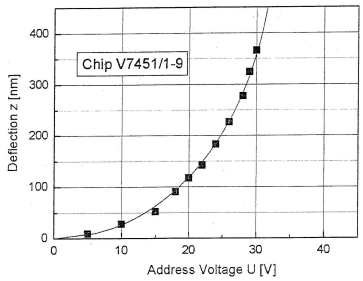

Figure 6.5: Curve of the deflection of a mirror segment depending on the applied voltage [FIP05] .

Amplifier for MEMS

Out of the 8×8 pixel groups, 40 neighbouring pixel groups were chosen to address them. First, the connections for the amplifier were prepared, disentangling the pin ordering on the board of the mirror. An amplifier with 40 channels, with an amplifying factor of 10 and a small rise time was designed and manufactured (Fig. C.1). The voltage of $\pm 12V$ for the supply of integrated circuits of the amplifier is delivered by a common computer power supply unit. The additionally needed $-5V$ come from a separate supply source.

6.2 Wavefront Sensors

In principle, for a closed-loop there is no need to know the absolute value of a wavefront aberration to correct it. It is sufficient to know how a wavefront has to be altered from the signal to get a planer wavefront. But to quantify the amount, that is the quality of the correction, a reference is needed. For that, the commercial interferometer and our Hartmann-Shack sensor were used serving as a reference for the new pyramid sensor.

6.2.1 Pyramid prism

The 3-sided pyramid prism was ordered in Changzhou, China. It is made of BK7 glass. The machining of this material benefits from most experiences and a variety of available devices to work it.
No coating was deposited on the surfaces.
The side length of the prism is 20mm with a base height of 4.6mm. The distance between base and tip measures 7mm. From this, the angle between the edges and the horizontal (or equivalent the base surface) of 11° and an

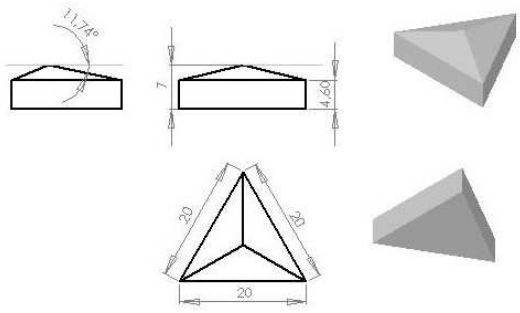

Figure 6.6: Dimensions of the 3-sided pyramid prism

angle between the symmetry axis line of the facets and the horizontal of 17.85° can be derived.

Figure 6.7: Topview on the tip of the 3-sided pyramid prism, unmounted and in it's holder.

Under a microscope, using an objective with long working distance, the edges and the tip could be examined. The width of the edges and the tip is smaller than $10\mu m$. A mounting which carefully holds the pyramid, was made to facilitate the implementation of the prism into micro-bench mountings.

Pupil collector

As the angle between the facets and the horizontal was chosen rather big to facilitate the production of sharper edges, the three split beams diverge stronger and cannot be imaged on one camera chip. Instead of taking the more complex and expensive solution of using three cameras, three mirrors were used as "pupil collector". Directly after the prism, the three mirrors reflect the three beams, so that the beam centres do not diverge any more. A compact mounting was made implementing three commercial beam splitter

holders, onto which the mirrors were fixed. The main angle correction is given by the mounting. Finer corrections can be done by means of the beam splitter holders which feature small screws for adjustment.

6.2.2 Interferometer

As reference wavefront sensor, the compact interferometer μ-*Phase* of Twyman-Green type from the company Fisba-Optik in St.Gallen, Switzerland, was used. The integrated source is a HeNe laser that is coupled via
a glass fiber to the interferometer components. The beam is divided by a beamsplitter, one beam being reflected at an internal mirror, the other beam leaving the interferometer to pass or to be reflected at the optical component of interest. Both beams are recombined by the same beamsplitter and detected by an internal CCD-camera with a transversal resolution of 61 pixel/μm. From the interference pattern, the wavefront aberrations are calculated by using a phase-shift procedure, where the internal mirror is moved five equidistant steps with a piezo-crystal.

6.2.3 ASIC Hartmann-Shack sensor

The Hartmann-Shack sensor chip used in this work was developed in our group by T.Nirmaier [Nir05]. A photodetector with an 8x8 subdetector array chip based on complementary metal oxide semiconductor (CMOS) technology was fabricated using silicon as photoelectric absorber. Each subdetector consists of 21x21 pixels. Here the displacement is determined by searching the centroid spot pixel. To obtain a high bandwidth, the deviation of the spot positions from centre was processed on hardware through application specific integrated circuits (ASIC). The sensor has thus the high frame rate of 362Hz. Defocus measurement with a resolution of 0.16 dioptre was achieved. Readout is done over a parallel port on a computer working under Linux operating system.
The lenslet array used has a focal length of $f = 53mm$. The lens arrangement matches with the detector pitch distance.

6.3 Light Sources

Two light sources were used. One was the built-in source of the interferometer, a HeNe laser working on the red line ($\lambda = 632.8nm$). The intensity of the coherent light is nearly continuously adjustable from $1\mu W$ down to zero. The beam was used with a diameter of 6mm as it was set for the other source, a superluminescence diode (SLD) with a bandwidth of $20nm$ and its

mid-wavelength in the infrared at $\lambda = 783nm$. While the HeNe laser has a coherence length of a few meters, the SLD exhibits a coherence length of only $30\mu m$, so that interference effects can almost be avoided.
The output power of the SLD had a fixed, non-adjustable value of $0.36\mu W$.

Focused beam radius
The focal length of the pyramid sensor's lens L_1 is $500mm$. According to Eq. (3.3) we can calculate a smallest limit for the spot radius of the focused beam onto the pyramid's tip, assuming negligible aberrations, of

$r_{Airy} = 1.22 \cdot 500mm \cdot \frac{783 \cdot 10^{-6}}{2 \cdot 3} \approx 0.08mm.$

Overview of all devices

DEVICE	SPECIFICATION
PC gotancad	Win2000; AMD AthlonXP 1800+, 512MB RAM
PC femtos	Win2000; x86 family6, 128MB RAM, 400MHz
PC everest	SuSE Linux9.0; AMD AthlonXP 1800+, 256MB RAM, 1160MHz
PC mohicanus	Win2000; Intel P4, 1GB RAM, 2,8GHz
PC interfero	Win98; Intel P I, 64MB RAM, 200MHz
D/A card	Lothar Bockstaller GmbH, 40 channels, 770Hz
frame grabber	IDS Falcon, CVBS, 6 to 30 frame/s
DM amplifier	home made
DM_m supply	Rohde&Schwarz Typ NGM 280/0.1
HSS supply	Voltcraft DC power, 2x 0...30V / 2,5A
CCD-camera	jAi Mechademic Company, CV-M300 monochrome, 8.8mm x 6.6mm, 752x582 pixel
ASIC-HSS	8X8 subdetectors, each with 21x21 pixels, >362Hz frame rate
DM_s	Fraunhofer Inst. IPMS ; $z_{max} = 0,4\mu m$, $40\mu m$x$40\mu m$ each mirror, 15x15 mirror = one controllable mirror group, 8x8 groups
DM_m	OKO Techn. Delft, 37 pistons, membrane, 500Hz, $9\mu m$ deflection
PP	customized by DDM Company, Changzhou, China
lenslet array	Adaptive Optics Associates; $400\mu m$ pitch distance, f=53mm

6.4 Software

The controlling of the system had to be done using two computers. The reason for this was, that it was not possible to integrate the available D/A-card for controlling the mirror in the same computer as the Falcon frame grabber video card due to restrictions of the Falcon's driver software. Thus two computers were connected with each other for data acquisition, that is to obtain a training set of input and output values.

Written in the programming-language C++ with Borland Builder 6, the program `camera.cpp` controls the mirror from computer1 (PC gotancad). In a real-time image of the pupils the size and position of the 3 circles[2] can be positioned manually. This defines the area that is saved out of the complete CCD read-out frame in each data acquisition cycle. `camera.cpp` sends the piston position information for each mirror deformation to computer2 (PC femtos). Both computers are directly connected via a LAN-cable. The D/A-card is addressed with a second program, called `deformablemirror.cpp`. Random piston combinations were produced and saved before in a file.

One acquisition cycle (that is acquisition of one input-output pair for the NN) consists of the following steps: From the mentioned file with the random combinations, computer1 reads out one piston combination; this data is sent to computer2 controlling the D/A-card. The 20 output voltages (19 voltages for the pistons and 1 for the membrane) are amplified and applied to the mirror. The CCD-camera is then read out by the frame-grabber card in computer1 and the selected area is saved to a file. Having completed the last step, the next cycle can start.

6.5 Structure and algorithm of the neural network

The NN was written under Matlab, version 7, with the Neural Network Toolbox package.
The designed NN is a convolutional NN. It is composed of two subnetworks: the preprocessing auto-encoding part of the net (the S_C-net) and the feed-forward backpropagation net (the BP-net).

The S_C-net consists of 2×4 layers. Starting with the first layer being a so called C-layer, the second being a so called S-layer, the third layer a C-layer, and altering in that order until the 8th and last layer which is a S-layer. The C-layers are layers with planes that were produced by simple averaging kernels out of the corresponding previous layers. The S-layers emerge from the previous layers by application of kernels, that have to be modified in the auto-encoding process. The size of these kernels has to be defined like the architecture of the net, but the values themselves emerge from training like the weights of a BP-net.

The number of planes in each layer is 36 except the first C-layer having 3 layers. The number of kernels in each layer is the same, as to each plane there is its corresponding kernel. The size of the planes varies between 2 and 22 (that means 2×2 and 22×22). The sizes of the kernels are 1×1, 2×2,

[2] instead of saving 3 circles, 3 squares fitting around the circle area are saved; this simplifies the image pre-processing that follows

layer	1(C)	2(S)	3(C)	4(S)	5(C)	6(S)	7(C)	8(S)
number of planes	3	36	36	36	36	36	36	36
size of plane	22	22	11	11	5	5	2	2
size of kernel	-	3	2	3	2	3	2	1

Table 6.1: Structure of the pre-processing network

or 3×3. In one and the same layer the size of all planes is identical and the size of all kernels is identical.

First the kernels of the S_C-net are modified by auto-encoding. When this self-organization has finished the BP net is trained. The pre-processing net has as output 36 small "planes" of size 2×2. This is the input of the BP net. An exception are the kernels of the first S-layer. They are special feature kernels (border kernels) and are not changed by the auto-encoding process.

The BP-net is a 3-layer, fully-connected feed-forward network. The hidden layer has 30 neurons. The output layer has n_{steps} neurons, where n_{steps} is the number of discrete height levels that are used for the mirror's pistons and was either 5 or 19. On the one hand 5 piston levels were chosen to have a relatively small number of outputs and of piston combinations and to cover in this way a larger part of all possible outputs with a the same amount of training examples. On the other hand the representation of Zernike polynomials was quite limited and taking a smaller number of levels would make no sense.

19 piston levels were chosen as an approximation for continuous deflection of the pistons, but keeping at the same time the discrete output value structure of the net.

The 5 or 19 output values are binary values in a so-called winner-take-it-all configuration; hereby all outputs can take a temporary value between 0 and 1, but it is the output with the highest value that will have the actual output 1, all other outputs becoming 0. This means, that only one of the 5 (or 19) outputs is "on", representing the correct height level .
The above BP-net regulates one single piston. Seven equivalent nets are trained, for each piston one BP-net.

The hyperbolic tangent sigmoid function tansig(x), which resembles the sigmoid function, is used as transfer function in both neuron layers (the hidden and the output layer) of the BP-net:

$$tansig(x) \quad = \quad \frac{2}{1 + e^{-2x}} - 1$$

As learning procedure the conjugate gradient back propagation method is used with the Beale-Powell reset condition.
The maximum epoch number is set to 10000.

The network presented here is one that showed best training results. Other nets, with different sizes of planes in the S_C-net, with less S_C-layers or with different numbers of neurons in the hidden layer of the BP-net were also trained.

The used structure can be summarized as follows:
From the single input layer, the first of eight layers of the self-organizing net emerges by convolution with twelve border shaping feature kernels. 2×2 subsampling is applied in between the four S-layers. The output of the last layer of the self-organizing net is the input of each of the seven 3-layer BP-networks. There will be only one "on" output from each net, representing the height level of the corresponding piston. The height levels of all 7 BP-networks give the discrete piston values of the wavefront that was produced (for training) or that has to be produced (for correction in closed-loop) by the pistons of the deformable mirror.

Chapter 7

Results

First practical experience with a confocal scanning laser ophthalmoscope (SLO) was made during a four month research stay in the Institute of Ophthalmology of the Moorfields Hospital in London.

Although the chronological order was different, the research which was carried out in London will be shown first as a motivation for how image acquisition can benefit from adaptive optics. Afterwards the work done on the pyramid sensor in Heidelberg is presented.

7.1 Polarisation Differential Imaging

A Zeiss SLO has been altered to allow for polarization differential (PD) imaging. The target is to investigate the possibility of recognizing diseases that affect the birefringent components of the fundus: the retina nerve fiber layer and the outer plexiform layer.

The modified SLO scans the eye with unpolarized light and is able to compare the image of the retina acquired from light linear polarized in one (arbitrary) direction with the image from light linear polarized perpendicular to the polarization of the other image. This comparison is done by subtracting one image from the other which means subtracting the recorded digital intensity values (grey values) of both images pixel by pixel. This must happen in real-time. For this reason, the back-reflected light was separated by a polarization beam splitter in two perpendicularly polarized signals and measured by two photomultipliers.

The SLO was a confocal SLO from Zeiss. The retina image acquisition was done by scanning the laser spot on the retina with a frequency according to PAL video standard, i.e. each second 25 pictures are scanned. One picture is composed of two frames: The first frame scans 313 lines, the second

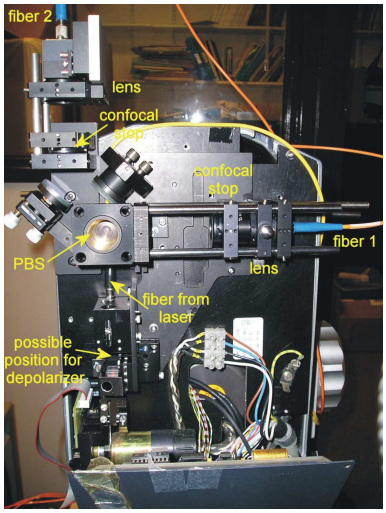

Figure 7.1: Photo of the optical part of the Zeiss SLO. A depolarizer, a polarizing beam splitter (PBS) and a complete second detection path were added.

frame scans another 312 lines in between the lines of the first frame. The fast horizontal and and the slow vertical scans are performed by a turning polygon mirror and a vibrating galvanometer mirror, respectively. The effective electronic acquisition time for one horizontal line signal is $4.7\mu s$. If a resolution of at least 200 points per line is desired, the bandwidth f_d of a device dealing with such a signal has to be $f_d > \frac{2 \cdot 200}{4.7 \cdot 10^{-6}} Hz = 85.11 MHz$! This criterion had to be fulfilled by the differential amplifier (DA) which had to generate the subtraction of both images. A differential amplifier from LeCroy (DA1855A) with a bandwidth of 100MHz could meet this requirement. We used the DA without amplification, that is with an amplification factor of 1. The image subtraction was done by inverting one of the two input signals (negative input) and then adding both signals.

Depolarizing the red diode laser ($\lambda = 635nm$) light was done using a quartz wedge depolarizer. This pseudo-depolarizer does not depolarize the beam completely. The degree of polarization dp (Eq. (2.1)) after the depolarizer depends on the beam intensity, on the beam diameter and on the angle between beam polarization and optical axis of the wedge. The best result is achieved when this angle is 45°. The used wedge depolarized a full polarized beam of 5mm diameter, to a $dp = 0.25$; it depolarized a beam of 2.5mm diameter to a dp of only 0.41. As space in the SLO's compact optical assembly was limited, it was not possible to expand the beam diameter of 2.5mm without having to rebuilt a big part of the assembly.

The red diode laser had an intrinsic dp of 0.53. This should result in a $dp = 0.53 \cdot 0.41 = 0.22$ after passing the wedge, which fitted to our measurement of $dp = 0.206 \pm 0.016$.

The detectors were two photomultipliers from Hamamatsu (R928), one from the modified SLO, the other taken from an identical SLO. Their signal outputs were the two inputs of the DA.

Figure 7.2 shows the whole signal path. The light returning from the eye is separated by a polarizing beam splitter into a beam with horizontal and a beam with vertical polarization. After the confocal pinholes two collimator lenses couple each beam into an optic fiber, leading the light to the photomultiplier. Their analog signals are compared by the differential amplifier whose output signal is digitized by a video card to a picture of 768x576 pixels. Thus, the differential image can be seen in real-time. However, if not only the differential image shall be recorded but also the two input images of the DA – in order to compare them with the differential image – the output channel of the DA has to be switched manually, causing a small time delay, during which the eye will usually change its position a bit.

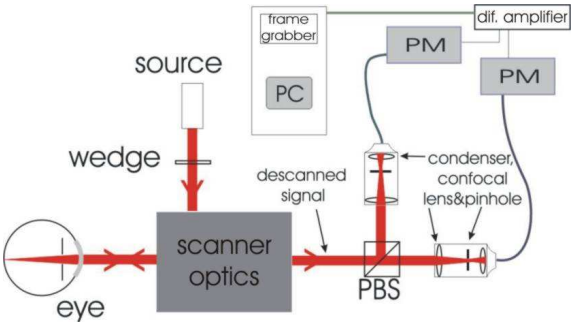

Figure 7.2: Scheme of the set-up for differential imaging. The reflected light of each scanned spot is divided at the polarizing beamsplitter (PBS) according to its polarization. Only light conjugated to the retina passes the confocal pinhole(s). The light is guided by glass fibers and the two intensities are detected by two photomultiplier (PM).

Measurements

Images of our own fundi and from eyes of colleagues were taken. This could be done with a $20° \times 20°$ or $40° \times 40°$ scanning field. The $40°$ range serves as an overview because the field includes the macula and the optic disc in one picture. Images of a $20°$ field acquire only a smaller area of the retina, but they have a higher resolution.

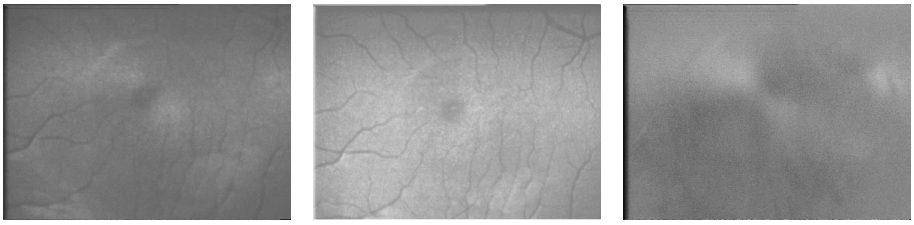

Figure 7.3: Differential images from the macula of S. (blue eyes). The left and middle image are the images from light of the two perpendicular polarizations. The right image is the differential image.

Contrast and brightness were adjusted manually with the photomultiplier electronics for each eye so that a good, not saturated or too dark, picture of the imaged fundus was provided.

Figure 7.4: Images of the optic nerve of C. (brown eyes). The right picture is the differential image of the left and middle picture.

The three images of Fig. 7.3 and the three images of Fig. 7.4 are taken with a delay of approximately 4 seconds between two images. Therefore the position of the eyes is not identical during the acquisition of the three images. It must be pointed out that in all cases the differential image was not calculated from the two images of perpendicular polarized light, but was measured directly.

Above pictures are the averaged images from 32 single pictures. This is done by a software that chooses a special feature of the pictures, a landmark like a blood vessel and aligns all 32 pictures according to this landmark. The vessel chosen should not be exactly straight, otherwise it is not possible to correct for transversal shifts but only for rotational movements. This averaging is the simplest way to improve signal to noise ratio. Still, the images are far away from their possible diffraction-limited resolution, as long as no adaptive optical system is compensating aberrations.

In the differential image of Fig. 7.3 the Haidinger brushes can be recog-

nized. This shows that differential imaging exhibits also information that is gained in standard polarimetry or ellipsometry[1] measurements. In the differential image shown in Fig. 7.4 features are brought out that are not visible in the two polarization images and thus would not be seen in a normal fundus image. The origin of these distinguished features is not clear but arouse strong interest in the physicians. Clinical trials shall follow.

Although it can not be seen immediately in above pictures, the contrast was increased by means of software in the later series, because the signal to noise ratio of an image from a bright (blue) eye is considerable higher than from a dark (brown) eye, as the former reflects more light.

7.2 First Sensing with a Pyramid Prism

A qualitative comparison between the ASIC Hartmann-Shack sensor and a 4-sided pyramid sensor in a modulation mode set-up was made on a short visit at the Max-Planck Institute for Astronomy (MPIA). The pyramid prism had turned edges of $12\mu m$ width. The circular modulation path of the beam around the prism tip was produced by a piezoelectric driven mirror with a modulation frequency of 200Hz. In Fig. 7.5 the image pupils for a wavefront

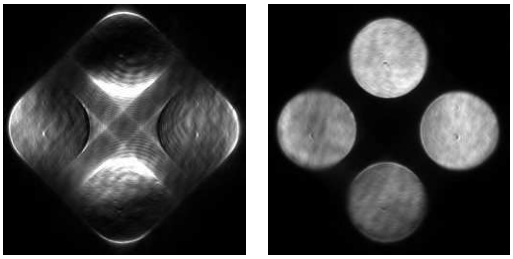

Figure 7.5: Pupil image of the 4-sided pyramid prism at the MPIA , in the left image unmodulated, in the right with modulation.

with coma can be seen: In the left image, taken with an unmodulated beam, the upper and the lower pupil are only illuminated at their inner borders where the pixels are saturated. The aberration amplitude of the coma is out of the pyramid sensor's range in unmodulated mode. Only when applying the modulation mode the signal of the large aberration is lying inside the linear range of the sensor.

[1] Ellipsometry is a special type of polarimetry (measurement of the polarization of light), where the polarization of light that is reflected from a thin sample (e.g. a film of layer) is investigated.

The Hartmann-Shack sensor showed a too small radiance sensitivity compared with a usual CCD camera even though the wavelength used was lying in the spectral bandwidth of maximum absorption of the silicon photodetectors. Approximately 70% of the wavefront intensity was supplied to the HSS and only 30% to the PS, but yet the signal to noise ratio of the HSS remained critical. Nevertheless, the correlation of Zernike polynomials up to the second order was given if the aberrations amplitude did not pass under a certain limit. Below this limit, where the aberrations were too small and the Hartman-Shack sensor was not sensitive anymore, the pyramid sensor was still detecting a clear signal.
Quantifying this limit with the own pyramid prism was the challenge.

7.3 Wavefront Sensing with all 3 Sensors

The measurement of a wavefront with the 3-sided pyramid sensor, the interferometer and the Hartmann-Shack sensor working in parallel and a quantitative comparison of their performance is not possible. The sensors exhibit different working ranges that overlap in their limits but prohibit a direct comparison. Their boundaries and limits are given in the following and it is indicated how they complement each other.
The membrane mirror is used as source of wavefront distortions and as actuator. Having two deformable mirrors, the original idea was to use one for producing random, temporally varying distortions and to use the other deformable mirror as actuator in the closed-loop for correction. This could not be realized as will be explained in the next section.

7.3.1 The MEMS mirror

Working with the HeNe laser as source for plane wavefronts in combination with the MEMS mirror produced a prominent interference pattern as strong side-effect.

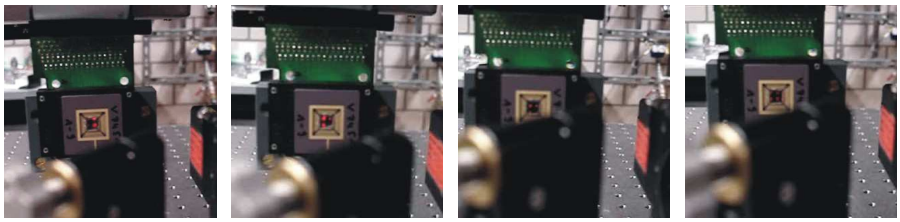

Figure 7.6: Pictures of a video sequence showing the interference effect of the MEMS mirror with a HeNe laser as light source.

The distance of the spots which form the interference pattern are measured in horizontal as well as in vertical direction for small angles from the normal direction to the mirror surface. A spot distance of 3±1mm is determined at a distance of 200±5 mm away[2] from the mirror. This is equivalent to an angle between two spots of 0.86°±0.15°. For the theoretically expected interference pattern from a mesh grid of infinite size, the interference maximum of n-th order is located at an angle $\alpha_n = \arcsin \frac{n \cdot \lambda}{g}$, with g being the grid constant. Inserting λ=633nm and g=40μm yields - for small angles, i.e. small orders - an angle difference of $\Delta\alpha = \alpha_{n+1} - \alpha_n \approx 0.91$. This value confirms the mirror elements being the origin of the interference effect.

Both pictures in Fig. 7.7 show the pupil images made with this mirror for two different and arbitrary wavefronts. A pattern change is recognizable, but the interference pattern dominates the whole image, making it impossible to use this signal for the training of a NN.

This pupil images look completely different – compared to the pupil image

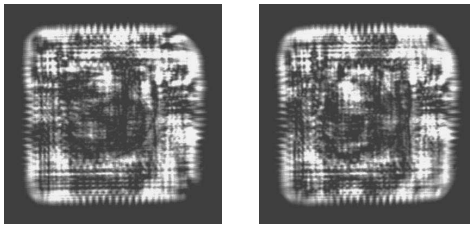

Figure 7.7: CCD-camera images of the MEMS mirror with different deformations. The interference pattern dominates as the mirror is illuminated by a high coherent HeNe laser.

made at the MPIA (Fig. 7.5) and to that made with the own set-up (Fig. 7.10) – due to two different set-up features, apart from using a segmented mirror (which still does not change the above statement): The image pupil beams were not separated with mirrors like it has been done in the own set-up (Fig. 7.10) and nearly overlapped in the image plane, making it possible to capture them with one CCD chip. Furthermore, the beam having a diameter of 6mm was illuminating the whole MEMS mirror. This is the reason for the pupils being of square shape. The MEMS mirror images were made with a 4-sided pyramid, by courtesy of the MPIA, before the ordered 3-sided pyramid prism has been delivered.

With the same optical set-up but the light source being the SLD the interference pattern faded but did not vanish completely. The coherence

[2] because of the built-up it was not possible to measure the distance to the mirror more precise

length of the SLD of approximate $30\mu m$ is still not short enough to avoid the interference effect caused by the segmented mirror. That is the reason why the idea of using the segmented mirror was abandoned.

7.3.2 Membrane mirror performance

For translating the applied piston height values on the membrane mirror to Zernike polynomials or, vice-versa, in order to know which positions the pistons have to take for a desired Zernike polynomial combination, a numerical least-square fit for non-linear functions under Matlab is used. The discrete

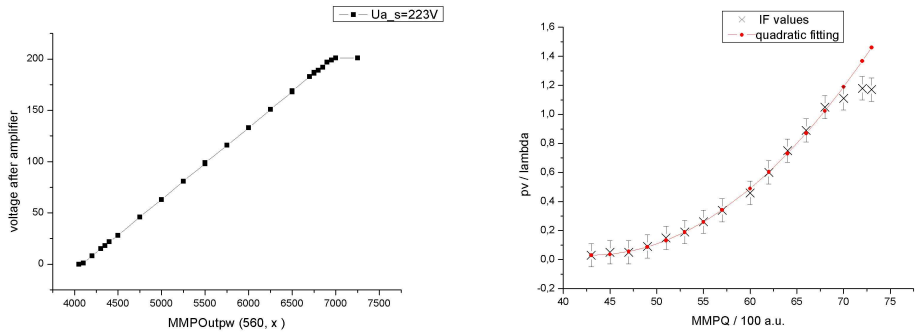

Figure 7.8: Relation between D/A converter output and mirror amplifier output (left) and D/A converter output and membrane mirror deflection (right).

piston positions of the inner 19 pistons are fitted to the first 10 Zernike polynomials, with the pistons 8 to 19 (see Fig. 6.2) having always one constant value.

At first, the deflection of the mirror in dependence on the driver software command value MMPQ (also called MMPOutpw) must be known. Therefore the range of the amplifier was verified measuring its output voltage in relation to the MMPQ values (Fig. 7.8, left curve). The curve on the right-hand was measured by means of the interferometer. One piston from the inner segment circle was chosen and different MMPQ values were applied to it and the peak-to-valley (pv) deflection between the raised piston and the surrounding circle was noted. The curve looks the same for every piston of the inner circle. If a piston from the outer circle is chosen, deflection can not be read out from the interferometer plot with exactitude. The reason of this and also of the big error bars in Fig. 7.8, is the uncertainty when reading the exact peak-to-valley value from the line plot (Fig. 7.9).
The quadratic relation between applied voltage and mirror deflection as

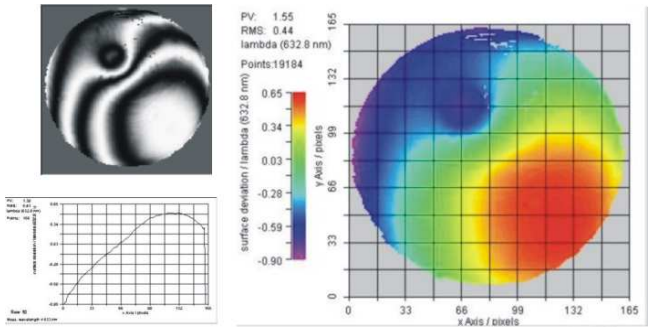

Figure 7.9: Interference pattern of the aberrated wavefront with the reference plane wave (top left) and the calculated contour plot of the wavefront deformation (right). The line plot (down left) is a selected vertical cut through the 2-dimensional colour-coded contour plot.

stated theoretically holds for MMPQ<6900. Above 6900 the amplifier is out of its linear range. That is why the output voltage from the amplifier saturates for higher values just as the deflection does.

7.3.3 Pyramid sensor images

For a plane, undistorted wavefront at the entrance pupil lens, the light intensity is evenly distributed over the pupil circles. The more aberrated the wavefront, the more the signal saturates according to the the pyramid's signal range.

Regardless of the sensor range, saturation can also arise from an inconvenient combination of beam intensity and camera read-out time. When using the HeNe laser, the intensity is adjusted by looking on wavefronts with aberrations at the limit of the sensor's measurable range, so that the signal is just not (completely) saturated. Since the SLD can not be adjusted, the read-out time of the CCD camera is adapted when using this light source. The infrared SLD light of the three beams after passing the pyramid prism has an intensity of less than 60nW. Read-out time of the CCD camera can be selected between $1/2000sec$, receiving hereby a nearly saturated signal, or $1/4000sec$, which yields a rather weak signal. We settled on a read-out time of $1/2000sec$ as it proved to be easier to train the net with pictures that show partly saturated pupil areas.

Figure7.10 shows the complete read-out of the CCD-camera capturing the three image pupils. In the left image the image pupils for a plane wavefront are shown. The right image is the sensor signal for an aberration with trefoil as main Zernike component. Three details can be seen:

First, the area between the pupils is not illuminated as the beams are separated and re-collected with the pupil collector. One gets rid of the light scattered from the edges into the area between the pupils of Fig. 7.5 (left).

Second, an interference pattern can be made out, which disturbs the pupil image. This pupil images were taken with the HeNe laser as wavefront source and the membrane mirror as actuator. Although the pupil images show clear and striking feature changes when applying different deformations on the membrane mirror, the interference pattern would make necessary a more complicate neural network in order to deal with this additionally given but useless information. Hence, the source was changed and the SLD was used as new source. Parallel reference measurements with the interferometer were not possible anymore, but the interference pattern – originating from

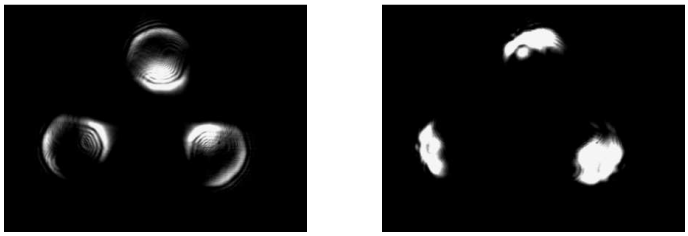

Figure 7.10: Pyramid pupil images, for a nearly plane wavefront (left) and for an aberrated wavefront (right).

diffraction on the entrance pupil and on the 6mm filter pupil directly after the source – disappeared.

The third noticeable detail is that the pupils are not homogeneously illuminated. The tip not being at the focal distance, as reason for this, can be excluded: the Rayleigh length (that is the length where the focused beam is the smallest and does hardly change its form)[3] is approximately 1cm for the given wavelength, focal length and beam radius.

The reason for the inhomogeneous illumination is the astigmatism and defocus deflection of the mirror when the used pistons are addressed to move to the same height. This deformation exists, because the outer piston ring is not used (resulting in an aberration with a defocus as main Zernike component) and because of the intrinsic, astigmatic deformation of the membrane as mentioned in section 4.1. Taking advantage of the neural network, the piston combination that would eliminate the astigmatism contribution was not applied, but this image was kept as corresponding NN input of the "plane"

[3]Rayleigh length b is given by $b = \frac{2\lambda}{\pi\theta^2 n}$, where λ is the wavelength, θ is the angle of divergence of the beam and n the index of refraction [Mes99].

piston output values. Thus, in closed-loop mode this is given as target. In the same way, the closed-loop system implemented in a SLO will be calibrated, i.e. an AO system with not perfect optics will have three not homogenous image pupils resulting from a given plane wavefront.
Besides, having for all pistons the same constant piston height as target has the (subjective) advantage that the mean square error (MSE) is calculated relatively to the same height for all pistons.

7.3.4 Comparison of the three sensors

Three criteria have been chosen to compare the sensors:

- the intensity range of the sensor that provides a signal to noise ratio in which the respective sensor can work
- the bandwidth, that is the time, the sensor needs to acquire the signal and to calculate the aberrations out of it and
- the spatial resolution and the resolution of the aberration's amplitude that the sensor is able to detect.

The signal intensity that the interferometer needs is given by the intensity of the reference arm. This can be altered in coarse steps by changing the internal reflection mirror or the objective. By doing so, the range can be adjusted in principle. The sensitivity is given by the internal camera, which can deal with intensities down to a few nW.
The resolution of the interferometer is $\frac{1}{100}\lambda \approx 0.6nm$. Although the interferometer is the sensor with the best resolution, it is beyond all question to use it for adaptive optics. The time to acquire the five required images for the 5-phase-algorithm and the additional calculation takes over 2 seconds. Some details (software implementation, mechanical stepping for the 5 images) that are obsolete could be improved. But still, the bandwidth that would be reached would be under the range of the fast Hartmann-Shack sensor or the pyramid sensor, both only requiring one image read-out and no mechanical parts to be moved.

The pyramid sensor in its actual configuration shows a bandwidth of less than 6Hz. Although a CCD-camera with a standard read-out frequency of 25Hz is used, this is not the limiting factor, but the very slow calculation and data process by Matlab that takes more than 90ms per wavefront, from data loading until the piston levels are calculated. The intensity sensitivity of the pyramid sensor is given by the camera and was in our set-up less than 15nW for an entrance pupil diameter of 6mm and an image pupil diameter

of 2mm. The spatial resolution is given by the diameter of the image pupils and is therefore not limited and adjustable to the resolution the mirror can deal with. The higher the desired or required resolution, the bigger is the number of inputs to the neural net and the training is more demanding.

The Hartmann-Shack sensor offers the fastest sensor by far with a bandwidth of over 300Hz. Its spacial resolution is given by the size of the microlenses of the lenslet which is $400\mu m$. Its aberration amplitude sensitivity or resolution is given by the focal length of the microlenses and the 21×21 pixels of a subdetector, resulting in a smallest mean deflection of $0.02°$of the wavefront that can be detected over one subaperture.
The limiting feature of the Hartmann-Shack sensor in its actual configuration in order to use it for application on the eye is its relative low light sensitivity. For an entrance pupil of 6mm diameter and an intensity of 70nW the signal-to-noise ratio is already quite critical.

7.4 Training of the Neural Network

For the acquisition of the training set the three selected pupil areas of the camera read-out frame were saved (as detailed in section 6.4) together with the piston voltage values applied therefore, these values being coded in units of the D/A converter driver software (MMPQ).

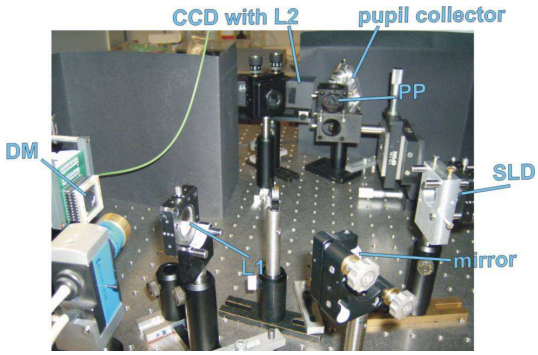

Figure 7.11: Photo of the set-up for acquisition of the training set and for the open loop tests.

The input values, that is each pixel grey value, had a range from 0 to 255. Any dependency on intensity fluctuations was avoided by normalizing this value. The output values, that is the piston heights, ranged between 4300 and 6200 (see Fig. 7.8). The range of the mirror was expanded into the lower range at the cost of partially leaving the linear interval of the mirror.

Only the 7 inner pistons were varied to obtain the training set and consequently, to correct the aberrations later on. The first tests were made

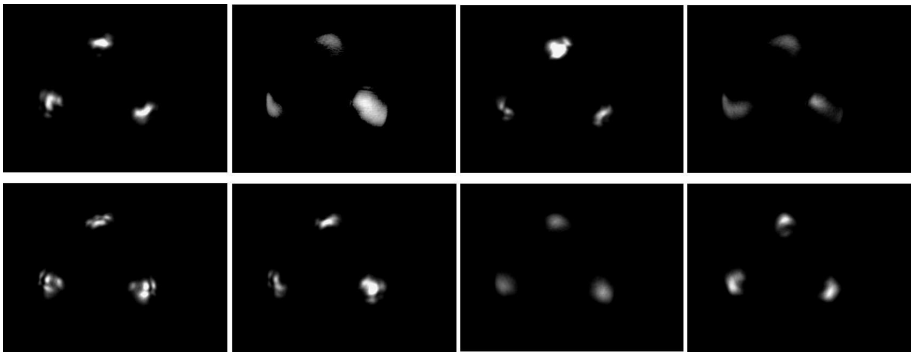

Figure 7.12: Extract from a sequence of the pupil image signals while different piston voltage combinations are applied to the mirror for acquisition of the training set.

with the 7 pistons being addressed with only 5 different discrete height levels (4700, 5000, 5300, 5600, 5900). This limited selection already offers 5^7=78125 combination possibilities. Afterwards, wavefronts of more continuous-like piston level combinations were presented to the net, with MMPQ=4300,4400, 4500, ..., 6100 (19 levels).
The voltage applied to the 12 pistons, piston 8 to 19, of the surrounding piston circle (actually a hexagon) was either for all MMPQ=4300 or MMPQ=5300. The outer circle formed by piston 20 to 37 was not defined, that is no voltages were applied to these 18 pistons.

When only 5 piston height levels (discrete levels) are used, performance is much 'smoother' than for 19 pistons heights (quasi continuous levels). With 19 piston heights, the performance improves greatly in the first epochs of training, afterwards the improvement becomes very slow, that is, the curve becomes quite flat (Fig. 7.13). Although training for both cases, with discrete and with quasi continuous levels, reaches a performance of similar values, the development of the training for 19 piston heights shows that the net is not optimal. Mean square errors between 0.17 and 0.21 are typically for the developed network architecture, but also MSE values of even 0.11 and 0.14 were achieved. This best performance was achieved in one of the latest setups with quasi continuous height levels.

Performance and beam alignment

The optical set-up was kept for all training sets gathered as shown in Fig. 7.11 and as explained at the beginning of chapter 6.

The pyramid prism is mounted on 3 micro-bench stages for translation in the direction parallel to the optical axis and in both transversal directions. This makes the positioning of the pyramid tip comfortable. The correct po-

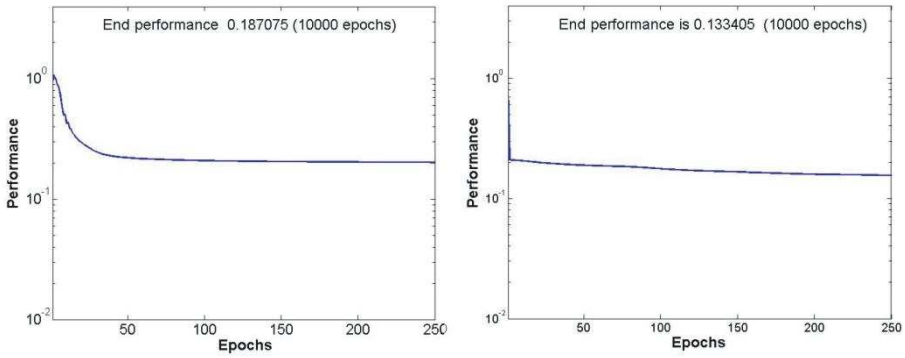

Figure 7.13: Training performance with 5 discrete height levels (left) and with 19 height levels (right).

sition, i.e. the position where the tip is in the middle of the focused beam spot, is found by looking at the appearance of the pupils in the image plane. The position of the symmetry axis of the pyramid which should be collinear to the optical axis can not be controlled. Further, its absolute position, that is the angle between the optical axis and the pyramid symmetry axis (or equivalent: the angle between the pyramid's base and the plane perpendicular to the optical axis) can only be estimated with a precision of $\pm 3°$.

A disadvantage of the micro-benches is their drifting after they are positioned. Especially the vertical micro-bench drifts noticeably due to gravitation. This was tried to evade by positioning the pyramid iteratively, with smaller and smaller steps to its end position. Data acquisition for the training set takes many hours and a drifting between up to $2\mu m$ in one hour could be observed and compensated with fine readjustment by means of a reference picture of the image pupils at the starting position.
Obviously, training sets where the drifting was large and not controlled implicated a worse learning performance. One training, where the vertical drifting reached $2\mu m$ deviation from the starting position while the acquisition of the training set yield a performance MSE of 0.29.

The option to use an additional tilt mounting to align the symmetry axis of the pyramid is not recommendable. A superimposed drifting of this mounting to those of the micro-benches can not be distinguished, and thus, not be corrected definitely.

The training performances with MSEs between 0.11 and 0.21 stem from 3 different (re)alignments of the pyramid prism and the optics following the pyramid and are independent of the applied height levels on the piston (i.e. discrete or quasi continuous heights). Remarkable is the fact, that the best MSEs stem from that alignment with the (subjectively) worst looking, because less homogeneous, pupil images for a plane wavefront.

Performance and noise

Above drifting can be regarded as a kind of mechanical noise. The net is presented slightly different pictures for the same piston heights combination. Data acquisition with different room light conditions were tested. Images were taken in a completely shaded room with normal room light and with variation of both within a set. Although the illumination conditions could be distinguished in the images, this did not affect distinctly the neural network's training performance (the MSE variance of three training runs was 0.01). This insensitivity to illumination noise can be attributed to the feature extraction by the image pre-processing and to the scaling of the pupil's pixel grey values.

7.5 Open Loop

Successful training performance lays in most cases between 0.17 and 0.21 MSE. But to know if the network really represents the given system, it has to pass the significant test with new input-output pairs that have not been part of the training set. Four hundred different test wavefronts have been presented to each trained network, to test if each one is able to predict the outputs of unknown inputs.

The network calculates for a given test wavefront the piston heights according to the 'learned' weights. The network's output is used to calculate the difference between current piston heights and the desired piston heights for a plane wavefront. This is subtracted from the anterior piston values and the following new wavefront signal is used as new input value. For closed-loop the same procedure is used, except that there is an intermission between evaluation of the signal and application of the new calculated deflection on the mirror because of the two computers and the two software programs that

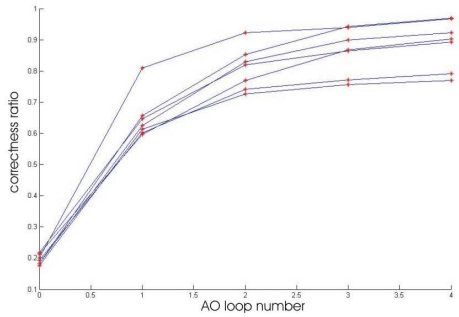

Figure 7.14: Single piston error

have to be used.

Not being a real closed-loop – I call it open loop – the correction factor[4] can be set to 1. In a real closed-loop realization the correction factor has to be reset, as the membrane of the deformable mirror, like all mechanical parts with inertia and the ability to oscillate, will affect the system's performance. The correction factor must be adjusted depending on the membrane resonance frequencies and the applied closed-loop frequency.

Figure 7.14 shows the evolution of the correctness ratio of all 7 trained pistons for 4 loops in the case of discrete piston height levels. The correctness ratio is the ratio of the number of wavefronts where the respective piston value was predicted right by the network and the total number of tested wavefronts (that is 400). Figure 7.15 describes the loop performance of the

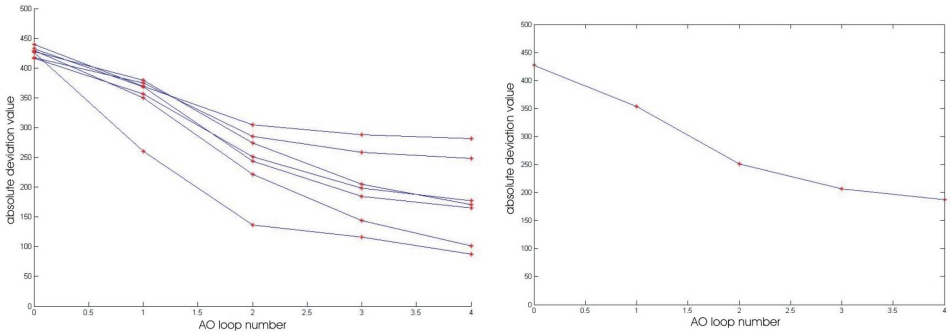

Figure 7.15: Loop performance for a net trained with 5 discrete height levels

same trained network in terms of absolute deviation in MMPQ units. The

[4]The correction factor is a number between 0 and 1 that is multiplied to the difference between the present actuator value(s) and the must value(s) to smooth the correction process.

plane wavefront was set to MMPQ=4300. Note that because of the quadratic relation between the MMPQ value and the actual deflection of the piston as shown in Fig. 7.8, the equivalent curve for absolute deviation performance in length units will have a steeper slope.

The loop performance of a trained network for quasi continuous height levels is shown in Fig. 7.16. Two pistons exhibit a markedly worse performance. This distinct behaviour was due to the pyramids position and remained in similar way for all loops made with this beam alignment. The reference plane wave was put at MMPQ=5300.

A very simple but strict evaluation figure is the total correctness ratio shown in Fig. 7.17. The total correctness ratio is the ratio of the number of completely plane wavefronts, i.e. where all 7 pistons have the correct height position, and the number of tested (i.e. corrected) wavefronts. The

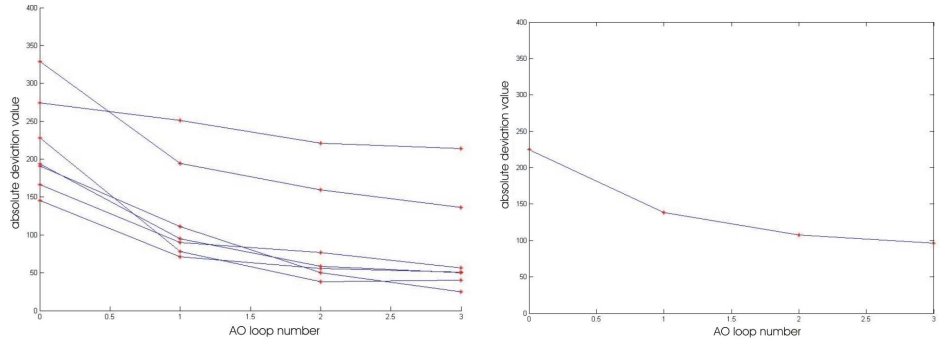

Figure 7.16: Loop performance of a net trained with 19 height levels

curve stems from the best achieved open loop performance in the discrete piston height levels mode. For the quasi continuous case with 19 height values for seven pistons, this is obviously a very demanding ratio and hardly no wavefront of the 400 presented wavefronts could show to be completely plane after the last open loop.

Calculating the RMS error of the test wavefronts before open loop and after the last loop in units of μm by taking into account the position of the reference plane wavefront reveals that the correction of all successfully trained nets is similar. The presented wavefronts exhibited a mean RMS error of 139±11nm for the discrete heights mode and a mean RMS error of 164±13nm for the quasi continuous heights mode. After correction the residual RMS was 51±11nm and 76±13nm respectively, where the RMS error for quasi continuous height values included networks that were trained with more noisy data.

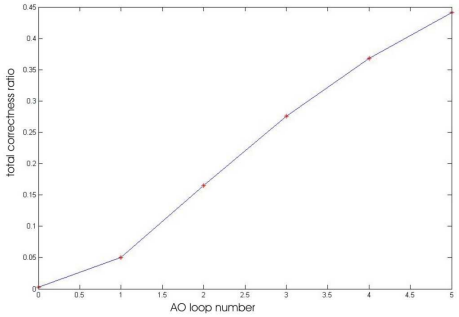

Figure 7.17: Ratio of the number of completely plane wavefronts to the number of the corrected wavefronts

The wavefront deformation could be reduced in both cases in average to less than half its starting RMS error.

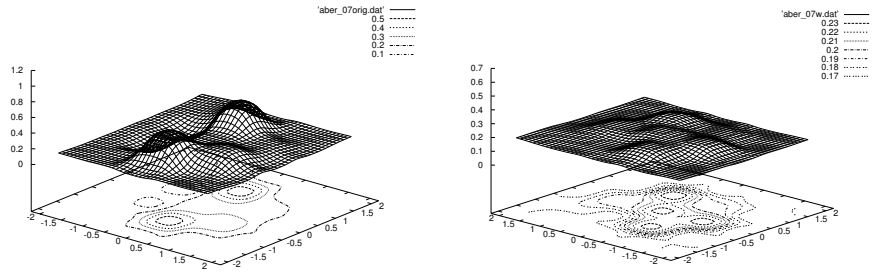

Figure 7.18: An aberrated wavefront as presented to the network (left), and after 4 correcting open loops (right). The z-axis' unit is in μm, the x- and y-axis are plotted in units of piston distances of the membrane mirror, that is 1.75mm.

Figure 7.18 shows as example one aberrated wavefront before and after open loop correction. The wavefront is one of the 400 test wavefronts presented to a neural network for quasi continous height levels and is one of the better corrected wavefronts. It was presented to the adaptive optical set-up having a RMS error of $135\pm13\mu$m. After 4 loops the wavefront was corrected to a RMS error of $50\pm13\mu$m.

7.6 Variations

Different parameters of the neural network can be changed, all affecting its performance and its ability to predict new wavefronts. Enhancement of the

first successfull networks was tried, first of all, by variation of the number of neurons.

Hidden layer

The neural network was tested with a different number of neurons in the hidden layer of the BP-net for the quasi continuous heights level mode. For a hidden layer with 10 neurons the performance curve shows a multi-step-like development within the first 20 epochs, passing then over to a very flat, hardly improving curve performance with a MSE after 10000 epochs of 0.187 . With 50 neurons, the performance yields a good progress in the first 6 epochs passing over to a flat, but still slightly falling curve part reaching a MSE of 14.2 after 10000 epochs of training. The performance progress for the networks with 70 and 100 neurons in the hidden layer is similar, also reaching a similar final error, with a MSE of 0.13 (Fig. 7.13, right curve) and a MSE of 0.12, respectively. Doubling the number of hidden layer neurons from 50 to 100 brings only a slight improvement. It can be assumed that with a number of neurons between 50 and 100 the net can represent the task. As a too large number of neurons is a risk for overfitting too, a neuron number below 70 neurons is a sufficient and more secure number.

Training set

Increasing the number of presented input-output examples can only improve the network's ability to predict a new pattern, provided that the example set is randomly distributed and that it covers the complete possible range. Training with 18000 input-output pairs was possible on a 1GB RAM computer (mohicanus). Training time for 10000 epoches and 18000 examples is 20 hours. An input-output set training of 20400 examples exceeded the memory capacity and a computer with 1.5GB RAM had to be used.

First tests were also made where the learning rate was changed between 0.8 and 1. Also, a parameter that correlates adjoining pistons was introduced. But no recognizable improvement was made out when varying this two parameters.

Chapter 8

Discussion

8.1 Performance and Limits

The performance of the neural networks shows that a neural network can learn the correlation between image signal of the pyramid sensor and the corresponding piston elevations. The reduction of new arbitrary wavefront distortions (laying within the sensitivity range of the sensor) to half the root mean square error after four to five loops shows further, that the network has actually been generalized to recognize the wavefronts for the correction task. Training performance as well as the correction are not optimal, though.

As the training performance for the 19 heights modus shows a good enhancement in the beginning, slowing down enhancement abruptly, a possible reason can be the limited or improper feature extraction from the S_C-net. The image pre-processing being able to extract the basic features but not the finer ones is one possibility, or the kernels being of improper type.

Tests to improve the performance can be carried out, like the following ones:
First of all the training set, that is the number of input-output examples, can be increased. A longer lasting training time is not relevant, as the network is trained only once, after the optic has been placed and does not need to be repeated again as long as the optic is not moved. Obviously, the RAM of the computer has to be of sufficient size. A translation of the neural network software to another more adequate language would support this demand, as calculations in a language which is not based on linear algebra expressions will diminish memory space. In addition, the calculation of the outputs would be performed faster after a successful training of the net, resulting in a higher bandwidth of the whole closed-loop.

Generally spoken, nowadays the computation power is no limit anymore

when applying neural networks for a closed-loop system, not even for a sensor like the pyramid prism which requires time consuming image pre-processing. In fact, a few years ago this was a limitation. Only sensors like the Hartmann-Shack sensor, with a simple relation between the signal and the wavefront aberration – a linear transformation in the case of the HSS – could be taken into consideration. The first who built a neural network for controlling between an actuator and a sensor was Vdovin in 1995 [Vdo95]. He used a network for the signal of a curvature sensor. With a limited spacial frequency of the aberration (as it is the case in this work too) by using a mirror with 4×4 pistons and two signal images of 5×5 pixel each, he already achieved a MSE of 0.2 μm. He had used 3000 training examples and the hidden layer of his 3-layer BP-net contained 16 neurons. However, he did not work with real, experimental input-output pairs, but with calculated pairs from a numerical model.

The increase of the training set will 'prepare' the network better for unknown wavefronts, provided that the network offers a structure that is capable to represent the task. In the BP-net the most effective parameter to vary is the number of neurons in the hidden layer.

The structure of the preprocessing S_C-net offers more parameters to be altered. Especially the kernels play an important role and have not been tested, that is modified, in this work. The promising challenge is to find the kernels matching to the characteristic feature of the signal image, so that a considerable improvement of the training performance arises.

Instead of the proposed trial-and-error method by changing the parameters we can think of other ways for a network improvement based on an examination of the learning process. It would consist in checking if the error function has side minima that cause problems or if the cigar-effect mentioned in section 5.2.1 is the reason for a flat performance curve. Further it would be important to inspect if the architecture is oversized.
These training details are not available for the neural network implemented in Matlab and therefore could not be checked.

The network was said to incorporate misalignments or aberrations inherent to the optical set-up. Any additional inherent aberration, reduces the remaining sensing range of the pyramid. For example, if the system exhibits an internal tilt in (+x)-direction, the wavefronts to be measured can have a larger tilt in (-x)-direction but only a small one in (+x)-direction, as it will reach the sensor's saturation range.

Likewise, imperfectness of the pyramid prism, like uneven surfaces or wide edges, cannot all be reconciled by a training of the network. Loss information on broad edges of the prism – that is loss of the information

about the aberrations of the small spatial spectrum – cannot be retrieved.

8.2 Conclusion and Outlook

The reduction of aberrations of 150nm root mean square error over a 6mm pupil to less than the half could be realized with this work with the first implementation of an artificial neural network as controller and a 3-sided pyramid prism as wavefront sensor of an AO system. The system shows a good ability to correct to its optimum within 3 to 5 loop steps as well as a high tolerance against background light noise.

A similarly correction can be expected in fast closed-loop performance. However, this can only be verified through an upgraded experimental set-up where the hardware controlling components, that is the frame-grabber card and the D/A-converter, are implemented in a single computer. Further, it is desirable to translate the actual neural network software to C or C++. Exportation out of Matlab is imperative as otherwise no bandwidth higher than a few Hertz will be achieved. With an additional integration of the controlling software in one program, control frequencies can be expected, that will just be limited by the read-out frequency of the CCD-camera.

The measurement and compensation of wavefront aberrations with the high-sensitive neural network pyramid sensor (NN-PS) system presented here has been shown for the unmodulated mode in order to measure dynamic aberrations of small amplitude. However, dynamic aberrations of larger amplitude than those which lie in the range of the NN-PS have also to be measured for an implementation of an AO scanning laser ophthalmoscope. The static, and usually largest aberrations are no handicap as they are compensated for each individual patient before image acquisition by positioning lenses (usually for defocus and astigmatism aberration). Static aberrations of Zernike orders above the second order can be compesated by phaseplates. It can be thought of two possible solutions to incorporate both scales: either to extend the actual neural network for application in the modulation modus in addition to the non-modulation modus, or to detect larger amplitudes of aberration with a second sensor measuring in that range, by construction of a two-stage sensor system. The later represents a rather complex and more expensive system, so that the former solution is the expedient one.

After a successful closed-loop operation, a transition of the NN-PS system from the laboratory table set-up into a SLO is a rather simple mission. It consists in adding a beamsplitter and two lenses (to measure in the conjugate plane to the eye's pupil) as 'connecting elements' between the ophthalmo-

scope and the neural network pyramid sensor system.

Appendix A

The layers of the retina

The retina is the inner coat of the eye ball with a thickness of approximately $250\mu m$. It is separated from the vitreous body by the inner membrane and from the choroidea by Bruch membrane (not indicated in Fig. A.1). Light has to pass several layers before it reaches the layer of the photoreceptors. In principle light is scattered at every layer. Focusing a confocal scanning laser ophthalmoscope to one layer will assist an imaging of that layer. Light

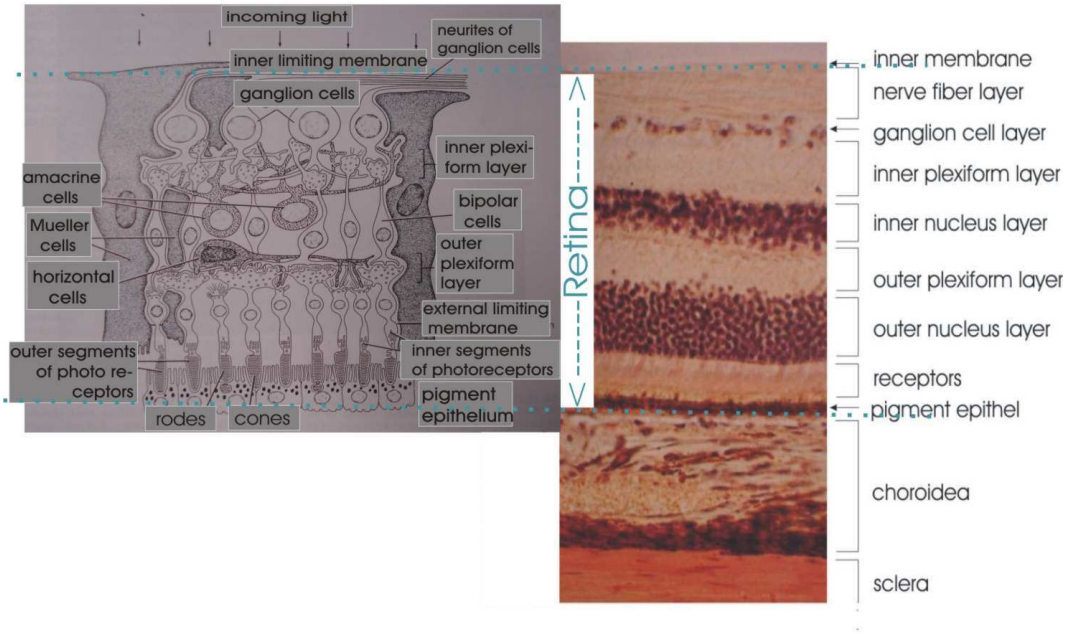

Figure A.1: The layers of the retina. Left: schematic picture; right: photo from a sectional cut (modified from [Jun96]).

that has been detected from the cones or from the rods is converted into an electro-chemical signal. The signal passes all retina layers (where the signals coming from the receptors are already preprocessed) in opposite direction back to the nerve fiber layers and to the optic nerve.

Appendix B

Zernike polynomials

The Zernike polynomials up to the $4th$ radial order are presented here. The nomination used in this work is the one established in ophthalmology, proposed by Thibos [Thi01]. Because it differs from the ISO-nomenclature, leading often to confusion, both terms are given in the second and third column respectively.

order	Z_k	ISO	$Z_k(\rho, \phi)$	aberration
0	Z_0	C_0	1	piston
1	Z_1	C_1	$2\rho \sin\phi$	y-axis tilt
1	Z_2	C_2	$2\rho \cos\phi$	x-axis tilt
2	Z_3	C_5	$\sqrt{6}\rho^2 \sin(2\phi)$	astigm. $\pm 45°$
2	Z_4	C_3	$\sqrt{3}(2\rho^2 - 1)$	defocus
2	Z_5	C_4	$\sqrt{6}\rho^2 \cos(2\phi)$	astigm. $0°/90°$
3	Z_6	C_6	$\sqrt{8}\rho^3 \sin(3\phi)$	trefoil $30°$
3	Z_7	C_7	$\sqrt{8}(3\rho^3 - 2\rho) \sin\phi$	y-axis coma
3	Z_8	C_6	$\sqrt{8}(3\rho^3 - 2\rho) \cos\phi$	x-axis coma
3	Z_9	C_9	$\sqrt{8}\rho^3 \cos(3\phi)$	trefoil $0°$
4	Z_{10}	C_{17}	$\sqrt{10}\rho^4 \sin(4\phi)$	
4	Z_{11}	C_{11}	$\sqrt{10}(4\rho^4 - 3\rho^2) \sin(2\phi)$	astigm. $0°$, 2^{nd} order
4	Z_{12}	C_8	$\sqrt{5}(6\rho^4 - 6\rho^2 + 1)$	spherical aber.
4	Z_{13}	C_{12}	$\sqrt{10}(4\rho^4 - 3\rho^2) \cos(2\phi)$	astigm.$45°$, 2^{nd} order
4	Z_{14}	C_{16}	$\sqrt{10}\rho^4 \cos(4\phi)$	

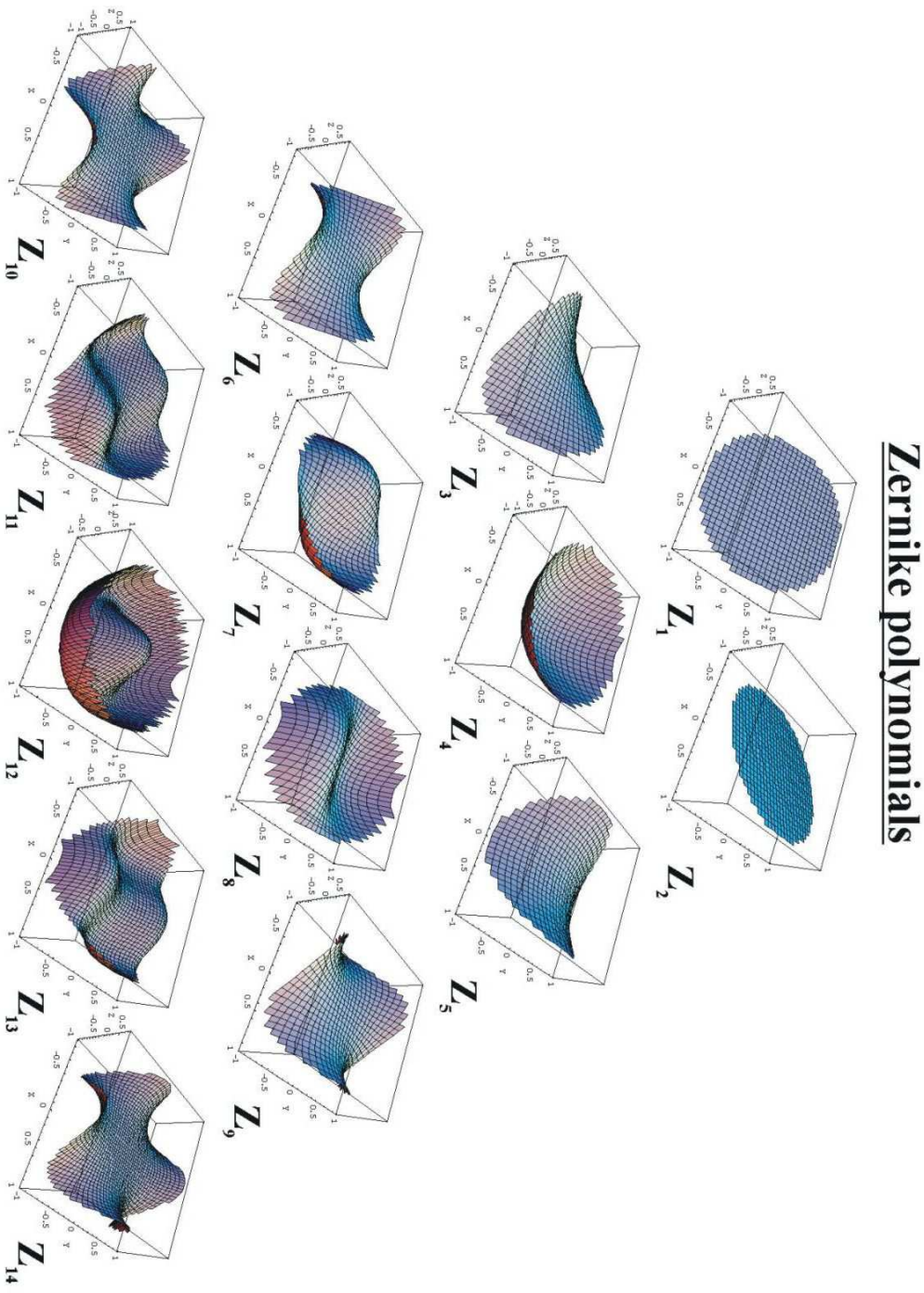
Zernike polynomials
Z1
Z2
Z3
Z4
Z5
Z6
Z7
Z8
Z9
Z10
Z11
Z12
Z13
Z14

Appendix C

Amplifier circuit diagram

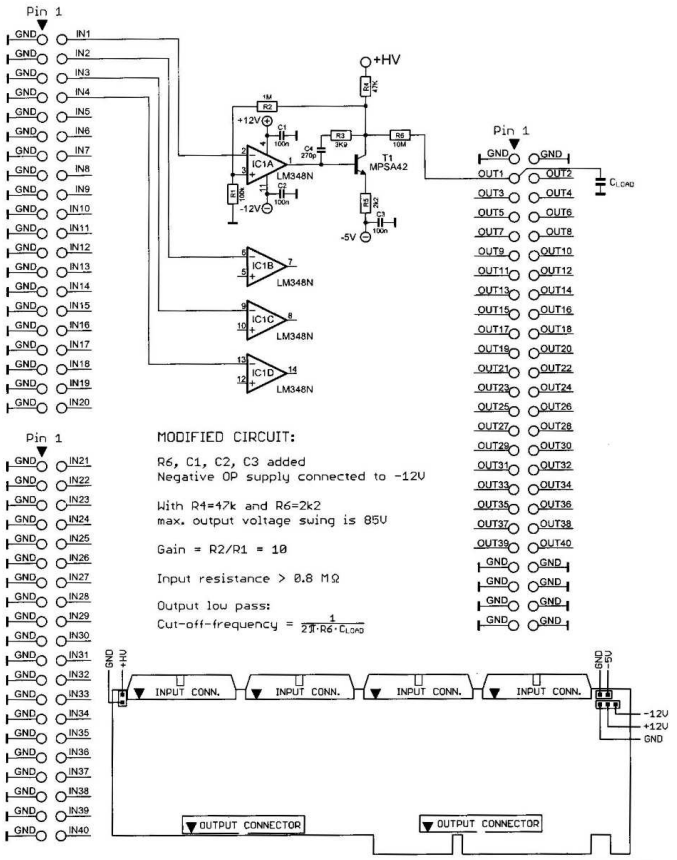

Figure C.1: Amplifier to address all 64 pixel groups of the MEMS mirror; built by the electronic workshop of KIP.

There are 64 integrated circuit (IC) amplification moduls integrated on the amplifier board. A gain of 10 is sufficient to amplify the D/A board signal between 0 and 5V to the control voltage of the segmented mirror of up to 35V. $\pm$12V provide the supply voltage for the ICs. The connected -5V shift the amplification range to negativ voltages in order to be able to actually amplify from 0V. The third supply (HV) is the source for the output gain voltage and should not exceed 35V to prevent a damage of the mirror.

Bibliography

[Art95] P.Artal, I.Iglesias, N.López-Gil, D.G.Green, *Double-pass measurements of the retinal-image quality with unequal entrance and exit pupil sizes and the reversibility of the eye's optical system,* J. Optical Soc. of America A **12** (10), p.2358 (1995)

[Ber03] T.Berendshot, P.DeLint, D. van Norren, *Fundus reflectance-historical and present ideas*, Progress in Retinal and Eye research **22**, p.171 (2003)

[BiL94] J.Liang, B.Grimm, S.Goelz, J.Bille, *Objective measurement of the wave aberrations of the human eye using a Hartmann-Shack wave-front sensor*, J. Optical Soc. Am. A **11** (1994)

[Bin06] A.Bindewald et al., *Classification of abnormal fundus autofluorescence patterns in the junctional zone of geographic atrophy in patients with age related macular degeneration,* B J. Ophthalmology **89**, p.874 (2005)

[BiN73] E.Bin-Nun, F.Dothan-Deutsch, *Mirror with adjustable Radius of Curvature,* Rev. Scient. Instruments **44**, p.512 (1973)

[Boj01] S.Bojanic, T.Simpson, C.Bolger, *Ocular microtremor: a tool for measuring depth of anaesthesia?*, British Journal of Anaesthesia **84** (4), p.519 (2001)

[Bue00] J.Bueno, *Measurement of parameters of polarization in the living human eye using imaging polarimetry*, Vision Science **40**, p.3791 (2000)

[Bur95] S.Burns, S.Wu, F.Delori, A.Elsner, *Direct measurement of human-cone-photoreceptor alignment,* J. Optical Soc. Am. A **12** (10), p.2329 (1995)

[Cas02] J.Castejón-Mochón, N.López-Gil, A.Benito, P.Artal, *Ocular wavefront aberration statistics in a normal young population*, Vision Research **42**, p.1611 (2002)

[Cha06] S.R.Chamot, C. Dainty, S.Esposito, *Adaptive optics for ophthalmic applications using a pyramid wavefront sensor*, Optics Express **14** (2), p.518 (2006)

[Cla03] R.Clare, R.Lane, *Wavefront sensing from spatial filtering at the focal plane*, Proc. of SPIE Vol.5169 (2003)

[Cos05] J.Büchler Costa, *Development of a new Infrared Pyramid Wavefront Sensor*, PhD thesis, Universität Heidelberg (2005)

[Dia03] L.Diaz Santana, C.Torti, I.Munro, P.Gausson, C.Dainty, *Benefit of higher closed-loop bandwidths in ocular adaptive optics*, Optics Express **11** (20), p.2597 (2003)

[Dub04] A.Dubra, C.Paterson, C.Dainty, *Study of the tear topography dynamics using a lateral shearing interferometer*, Optics Express **12** (25), p.6278 (2004)

[Eng96] M.Engdahl, *Phase Unwrapping in SAR Interferometry Using Instantaneous Frequency Estimation*, Helsinki University of Technology, Master Thesis 1996

[Esp00] S.Esposito, O.Feeney, A.Riccardi, *Laboratory test of a Pyramid Wavefront Sensor*, Proc. of SPIE Vol. 4007, p.416 (2000)

[Fer01] E.Fernández, I.Iglesias, P.Artal, *Close-loop adaptive optics in the human eye*, Optic Letters **26** (10), p.746 (2001)

[FIP05] Fraunhofer Institute for Photonic Microsystems, specification sheet of project no.202185

[Ghi03] M.Ghigo, F.Perennes, R.Ragazzoni, *Manufacture by deep x-ray lithography of Pyramid Wavefront Sensor for astronomical Adaptive Optics*, SPIE Proc. 4839, p.259 (2003)

[Gre02] J.Grebe-Ellis, *Zum Haidinger-Büschel*, Didaktik der Physik, Frühjahrstagung Leipzig 2002

[Goo05] J.Goodman, *Introduction to Fourier Optics*, Roberts Publishers 2005, 3rd ed.

[Guo06] H.Guo, N.Korablinova, Q.Ren, J.Bille, Wavefront reconstruction with artificial neural networks, Optics Express **14** (14), p.6456 (2006)

[HE04] Heidelberg Engineering, Heidelberg Retina Tomograph (2004); *www.heidelbergengineering.com/hrt.html*

[Hof01] H.Hofer, P.Artal, B.Singer, J.Aragón, D.Williams, *Dynamics of the eye's wave aberration*, J. Opt. Soc. Am A **18** (3), p.497 (2001)

[Hua03] X.Huang, R.W.Knighton, *Theoretical model of the polarization properties of the retinal nerve fiver layer in reflection,* Applied Optics **42** (28), p.5737 (2003)

[Hud03] C.Hudson, J.G.Flanagar, G.S.Turner, H.C.Chen, L.B.Young, D. McLeod, *Correlation of a scanning laser derived oedema index and visual function following grid laser treatment for diabetic macular oedema,* Br. J. Ophthalmology **87**, p.455 (2003)

[Igl02] I.Iglesias, R.Ragazzoni, Y.Julien, P.Artal., *Extended source pyramid wave-front sensor for the human eye*, Optics Express **10** (9), p.419 (2002)

[InsAl] Instituto Alcon; *http://www.institutoalcon.com/ia.asp*

[Jae97] B.Jähne, *Digitale Bildverarbeitung,* Springer Verlag 1997, 4.Aufl.

[Jun96] L.C.Junqueira, J.Carneiro, *Histologie,* Springer Verlag 1996, 4.Aufl.

[Kie03] E.Kierig, *Novel Control Algorithm for Real Time Adaptive Optics Systems,* Diplomarbeit, University Heidelberg (2003)

[Kor94] J.Koretz, D.M.Alberts, F.A.Jakobiec, *Principles and Practice of Ophthalmology,* Saunders Philadelphia 1994

[Kra96] J.van de Kraats, T.Berendschot, D. van Norren, *The pathways of light measured in fundus reflectometry,* Vision Research **36** (15), p.2229, (1996)

[Kri99] Krieglstein, Jonescu-Cuypers, Severin, *Atlas der Augenheilkunde,* Springer 1999

[Lia97] J.Liang, D.Williams, *Supernormal vision and high resolution retinal imaging through adaptive optics,* J. Optical Soc. Am. A **14**, p.2884 (1997)

[LeC89] Y.LeCun, B.Boser, J.S.Denker, D.Henderson, R.E.Howard, W.Hubbard, L.D.Jackel, *Backpropagation Applied to Handwritten Zip Code Recognition*, Neural Computation **1**, p.541 (1989)

[Lin05] Y.Lin, H.Carrel, I.Wang, P.Lin, F.Hu, *Effect of Tear Film Break-up on Higher Order Aberrations of the Anterior Cornea in Normal, Dry and Post-LASIK Eyes*, Journal of Refractive Surgery **21**, p.525 (2005)

[Mel06] Melles Griot: *http://www.mellesgriot.com/products/optics* and *http://glassbank.ifmo.ru/eng*

[Mes99] D.Meschede, *Optik, Licht und Laser,* Teubner Verlag Stuttgart 1999

[Mik73] S.Mikoshiba, B.Ahlborn, *Laser Mirror with variable Focal Length,* Rev. Scient. Instruments **44**, p.508, (1973)

[Neu98] C.Neubauer, *Evaluation of Convolutional Neural Networks for Visual Recognition,* IEEE Transactions on Neural Networks **9** (4), p.685 (1998)

[Nir03] T.Nirmaier, *A CMOS-based Hartmann-Shack Sensor for Real-Time Adaptive Optical Applications*, Dissertation, University of Heidelberg (2003)

[Nir05] T.Nirmaier, C.Alvarez Diez, J.Bille, *High-Speed CMOS Wavefront Sensor with Resistive-Ring Networks of Winner-Take-All Circuits,* IEEE J. Solid-State Circuits **40** (11), p.2315 (2005)

[Pat03] C.A.Paterson, *Lens and cataract*, Basic and clinical science course 2003-2004, American Academy of Ophthalmology

[Pis06] O.Pishnyak, A.Golovin, L.Kreminska, J.J.Pouch, F.A.Miranda, B.K.Winker, O.D.Lavrentovich, *Smectic-A-filled birefringent elements and fast switching twisted dual-frequency nematic cells used for digital light deflection*, Optical Engineering **45** (4), p.044002-1 (2006)

[Rag96] R.Ragazzoni, *Pupil plane wavefront sensing with an oscillating prism*, Journal of Modern Optics **43** (2), p.289 (1996)

[Rag99] R.Ragazzoni, J.Farinato, *Sensitivity of a pyramidic Wave Front sensor in closed loop Adaptive Optics*, Astronomy and Astrophysics **350**, L23-L26 (1999)

[Rag00] R.Ragazzoni, A.Ghedina, A.Baruffolo et al., *Testing the pyramid wavefront sensor on the sky*, Proc. of SPIE Vol. 4007, p.423 (2000)

[Ric98] A.Riccardi, N.Bindi, R.Ragazzoni, S.Esposito, P.Stefanini, *Laboratory characterization of a "Foucault-like" wavefront sensor for Adaptive Optics*, SPIE Vol.3353, p.941 (1998)

[Rod90] F.Roddier, *Wavefront sensing and the irradiance transport equation*, Applied Optics **29** (10) p.1402 (1990)

[Roo02] A.Roorda, F.Romero Borja, W.J.Donnelly III, H.Queener, T.J.Hebert, M.Campbell, *Adaptive optics scanning laser ophthalmoscopy*, Optics Express **10** (9), p.411 (2002)

[Rue98] A.von Rückmann, F.Fitzke, Z.Gregor, *Fundus autofluorescence in patients with macular holes imaged with a laser scanning ophthalmoscop*e, Br. J. Ophthalmology **82**, p.346 (1998)

[Rus95] S.Russell, P.Norving, *Artificial Intelligence - A Modern Approach*, Prentice-Hall London 1995

[Sch03] G.Schmidt, *Regelungs- und Steuerungstechnik*, Skriptum 2003, Technische Universität München

[ScE] E.Schöneburg, N.Hansen, A.Gawelczyk, *Neuronale Netzwerke,* Pearlson Education 1990

[Sot03] M.Soto, E.Acosta, S.Ríos, *Performance analysis of curvature sensors: optimum positioning of the measurement planes,* Optics Express **11** (20), p.2577 (2003)

[Thi01] L.Thibos, *Wavefront Data Reporting and Terminology,* J. of Refractive Surgery **17** (2001)

[Ver01] C.Verinaud, S.Esposito, *Real-time phasing and co-phasing of a ground-based interferometer with a pyramid wavefront sensor*, Meeting Venice, Beyond Conventional Adaptive Optics (2001)

[VdoS95] G.Vdovin, P.M.Savarro, *Flexible mirror micromachined in silicon*, Applied Optics. **34** (16), p.2968 (1995)

[Vdo95] G.Vdovin, *Model of an ada*ptive optical system controlled by a *neural network*, Optical Engineering **34**, (11), p.3249 (1995)

[Wue99] S.Wühl, *Aktive Korrektur optischer Aberrationen mittels Genetischer Algorithmen*, Diplomarbeit, Universität Heidelberg (1999)

[Zha05] H.Zhang, *Design of a Precompensation Unit Using Phase Plates For Lower-Mid Order Optical Aberrations of the Human Eye,* Master Thesis, University of Heidelberg (2005)

[Zho02] Q.Zhou, R.Weinreb, *Individualized Compensation of Anterior Segment Birefringence during Scanning Laser Polarimetry,* IOVS **43** (7), p.2221 (2002)

Acknowledgments

This work could be realized due to the help and support of many people. I am much obliged to everybody who in one way or another made a contribution to this work. It is my pleasure to name a few of them:
My special thanks go to

Prof. Bille, for giving me the opportunity to work with all liberty on this very interesting and interdisciplinary field of optical physics

Prof. Brenner who accepted to be referee of this dissertation

Feng, for his invaluable, "remote" advice and support, for the discussions we had and for sharing my enthusiasm for neural networks

Hongwei, with his calm and patient but efficient nature, for his help with the Borland Builder programming

Konstantin who dedicates more time than he has to help people – doing this with full devotion – and built us the fastest computer from the lowest-priced components

from the Max-Planck Institute for Astronomy, to Sebastian, Joanna, Daniela, Diethard and S.Hippler for the discussions and for sharing their experience with us

Prof. Fitzke, for supporting our ideas and my stay in the Institute of Ophthalmology in London

Vy who was an always-being-there assistance with the talent to provide or find every part that was needed in my host laboratory

Silke and Siri, for the pleasant working and living together in expensive-exalted-exciting London

Nick, for his help when I had 'conflicts' with my computer or (own) memory loss and for relaxed breaks at Botanik

DAAD which supported financially my stay in London

Mikael and Olivier, for discussions and a cosy laboratory co-working

Nina who makes an agreeable group working atmosphere being always in good mood

Sarah, for pleasant chats and for correcting my English

Line and Christina, for their assistance while their 'Miniforschung' and Master work respectively

Harald who not only provided me with good music and shares my passion for Tango but supported me with his valuable tips and advice concerning optics

S.Spiegel, for his helping hand in the mechanical workshop and for amazing me how many things there can be stored in a few small basement rooms

Heidelberg Engineering, for their very friendly cooperation

F.Balschbach for the bunch of black garbage bags that she handed out which were "misused" for a very helpful purpose

D.Weiskat, for the improvement of the amplifier and specially V.Kiworra, who insisted in hunting the loose contacts

Oscar, for the enjoyable breaks and chats and Barbara for her useful hints concerning the layout

Haiyan, Minyoung and Olivier, for all the affectionate and motivating support from afar

and to Enrique who taught me a lot about medicine and ophthalmology, who supported me and who showed me to have a different point of view of (not only) physicians.

My love and warmest thanks go to my family: mis padres que nunca han dejado de apoyarme en toda mi carrera (gracias!) and my brother, for proofreading and for all the other help and tips that he has given me all over the years.

Thank you!